This is the peer-reviewed, final accepted version for American Mineralogist, published by the Mineralogical Society of America.
The published version is subject to change. Cite as Authors (Year) Title. American Mineralogist, in press.
DOI: https://doi.org/10.2138/am-2021-7758. http://www.minsocam.org/

Revision 1

Raman spectroscopic quantification of tetrahedral boron in synthetic aluminum-rich tourmaline

Martin Kutzschbach[1*], Bernd Wunder[2], Iris Wannhoff[3], Franziska D.H. Wilke[2], Frédéric Couffignal[2], Alexander Rocholl[2]

[1]Fachgebiet Angewandte Geochemie, Technische Universität Berlin, 10587 Berlin, Germany

[2]GFZ German Research Center for Geoscience, Telegrafenberg, 14473 Potsdam, Germany

[3]Institut für Erd- und Umweltwissenschaften, Universität Potsdam, 14476 Potsdam, Germany

[*]E-mail: m.kutzschbach@tu-berlin.de

ABSTRACT

The Raman spectra of five $^{[4]}$B-bearing tourmalines of different composition synthesized at 700°C/4.0 GPa (including first-time synthesis of Na-Li-$^{[4]}$B-tourmaline, Ca-Li-$^{[4]}$B-tourmaline and Ca-bearing □-$^{[4]}$B-tourmaline), reveal a strong correlation between the tetrahedral boron content and the summed relative intensity of all OH-stretching bands between 3300 – 3430 cm^{-1}. The band shift to low wavenumbers is explained by strong O3-H…O5 hydrogen bridge bonding. Applying the regression equation to natural $^{[4]}$B-bearing tourmaline from the Koralpe (Austria) reproduces the EMPA-derived value perfectly [EMPA: 0.67(12) $^{[4]}$B pfu vs. Raman: 0.66(13) $^{[4]}$B pfu]. This demonstrates that Raman spectroscopy provides a fast and easy-to-use tool for the quantification of tetrahedral boron in tourmaline. The knowledge of the amount of tetrahedral boron in tourmaline has important implications for the better understanding and modeling of B-isotope fractionation between tourmaline and fluid/melt, widely used as tracer of mass transfer processes.

Keywords: Tourmaline, high pressure, synthesis, tetrahedral boron, Raman, SIMS

This is the peer-reviewed, final accepted version for American Mineralogist, published by the Mineralogical Society of America.
The published version is subject to change. Cite as Authors (Year) Title. American Mineralogist, in press.
DOI: https://doi.org/10.2138/am-2021-7758. http://www.minsocam.org/

INTRODUCTION

Tourmaline is considered an ideal indicator of the temperature, pressure, element- and isotope chemistry of its host environment. This is owed to its stability over a wide P-T-X range and the fact that it maintains its composition due to very low volume diffusion (Henry and Dutrow 1996). Tourmaline is the most important and widespread borosilicate in Earth's crust and hence its boron isotope composition is frequently used to reconstruct the temperature and fluid evolution of the hydrothermal system in which it crystallizes.

In recent publications the boron isotope record of tourmaline has been successfully applied as a thermometer in magmatic-hydrothermal W-Sn deposits (Codeço et al. 2019), as a tracer of fluid sources and pathways during alpine metamorphism of a sedimentary suite (Berryman et al. 2017) or to reveal the provenance of fluids associated with high-pressure metamorphism in subduction zones (Guo et al. 2019). Other examples include the work of Nakano and Nakamura (2001), Trumbull et al. (2009) or Bast et al. (2014).

In all these studies knowledge of the partitioning of the two stable boron isotopes ^{11}B and ^{10}B between tourmaline and fluid is crucial and it has been shown that it is mainly dependent on temperature and boron speciation in tourmaline (Meyer et al. 2008; Kutzschbach et al. 2017a). The boron speciation in the fluid has a minor effect, because tourmaline is only stable in near-neutral to acidic crustal fluids and under these pH conditions trigonal $B(OH)_3$ is considered the only relevant B-species (Schmidt et al. 2005).

It is now generally accepted that beyond the regular amount of three B atoms per formula unit (pfu) in trigonal coordination ($^{[3]}B$), tourmaline can incorporate significant amounts of excess boron at the tetrahedral site ($^{[4]}B$) by substituting for Si. Natural tourmaline with total B-contents ($^{[3]}B + {}^{[4]}B$) up to 4.23 B pfu have been described from numerous locations, mostly from high-P environments and for Al-rich stoichiometries (e.g., Ertl et al. 1997; Ertl et al. 2018). In accordance to the natural findings, $^{[4]}B$-bearing tourmalines have been

synthesized with olenitic (Schreyer et al. 2000; Kutzschbach et al. 2016) and rossmanitic[1] (Kutzschbach et al. 2017b) compositions up to a maximum of 5.53 B pfu.

Experiments have shown that the boron isotope fractionation between tourmaline and fluid is affected by the tetrahedral boron content, such that it increases tourmaline´s affinity for the light ^{10}B (Kutzschbach et al. 2017a). This is owed to the longer $^{[4]}B$-O bond compared to the $^{[3]}B$-O and had already been predicted by *ab initio* calculations (Kowalski et al. 2013). Consequently, in B-isotope studies involving tourmaline, the tetrahedral boron content in tourmaline must be considered in order to apply the correct fractionation factor. Unfortunately, the quantification of tetrahedral boron is not an easy task and many of the available methods, such as electron-microprobe analysis (EMPA), single crystal X-ray structure refinement (SREF), nuclear magnetic resonance spectroscopy (NMR), and secondary ion mass spectroscopy (SIMS) are very demanding in terms of sample preparation, data processing and often require the availability of suitable reference materials. By evalulating the Raman spectra of synthetic $^{[4]}B$-bearing olenite [olenite: $NaAl_3Al_6Si_6O_{18}(BO_3)_3O_3(OH)$] and rossmanitic tourmaline [rossmanite: $\square(LiAl_2)Al_6Si_6O_{18}(BO_3)_3O_3(OH)$], Raman bands associated with tetrahedral boron have been detected on the low wave-number side of the OH-stretching frequency region (Kutzschbach et al. 2016; Kutzschbach et al. 2017b).

Herein, three new syntheses of Na-Li-$^{[4]}B$-, Ca-Li-$^{[4]}B$- and Ca-bearing $\square$-$^{[4]}B$-tourmaline with varying amounts of tetrahedral boron are presented. For simplicity, in the following we name these synthetic tourmalines elbaitic, liddicoatitic and Ca-olenitic tourmaline, respectively. A detailed characterization of the different proportions of end-members, following the IMA Commision classification (Henry et al. 2011), is given later in the chapter “EMP- and SIMS-analyses”.

[1]This tourmaline is best described as solid solution between “$\square$-Li-O root name” $\square Li_{0.5}Al_{2.5}Al_6Si_6O_{18}(BO_3)_3(OH)_3O$ (Henry et al. 2011) and the hypothetical end member $LiAl_3Al_6(B_3Si_3O_{18})(BO_3)_3(OH)_4$

This is the peer-reviewed, final accepted version for American Mineralogist, published by the Mineralogical Society of America.
The published version is subject to change. Cite as Authors (Year) Title. American Mineralogist, in press.
DOI: https://doi.org/10.2138/am-2021-7758. http://www.minsocam.org/

In conjunction with the previously synthesized $^{[4]}$B-bearing tourmalines, it is shown that the summed integrated Raman intensity of bands between 3300-3430 cm^{-1} and the $^{[4]}$B-content form a well-defined trend, which is used to calculate the tetrahedral boron content of natural tourmaline with an accuracy and precision comparable to the accuracy and precision of electron microscope analysis. Our results demonstrate the feasibility of Raman spectroscopy for the rapid and non-destructive quantification of tetrahedral boron in tourmaline without the need for standards or special sample preparation.

EXPERIMENTAL METHODS

Tourmaline synthesis

Experiments on the synthesis of three $^{[4]}$B-bearing tourmaline of various compositions were all performed at 700°C and 4.0 GPa in an end-loaded piston-cylinder press. Elbaitic tourmaline was synthesized in the system Na_2O-Li_2O-Al_2O_3-SiO_2-B_2O_3-H_2O (NLASBH), liddicoatitic tourmaline in the system CaO-Li_2O-Al_2O_3-SiO_2-B_2O_3-H_2O (CLASBH), both in 7-days-runs, and Ca-olenitic tourmaline in the system CaO-Al_2O_3-SiO_2-B_2O_3-H_2O (CASBH) in a 6-days-run. The starting materials in all three experiments consisted of γ-Al_2O_3, H_3BO_3 and SiO_2; as additional solid component for the experiments in the NLASBH- and CLASBH-systems we used Li_2O. For the experiment in the NLABSH-system, the solid starting bulk composition corresponds to the stoichiometric proportions of ideal elbaite end-member $[Na(Li_{1.5}Al_{1.5})Al_6(Si_6O_{18})(BO_3)_3(OH)_4]$, but with an excess of 100 mol % H_3BO_3 and 60 mol % Li_2O. 15 mg of the homogeneously mixed starting material was added together with 2 ml of 6.1 mol/l saturated NaCl-solution into a gold capsules of about 10 mm length and 3 mm in diameter. For the experiment in the CLASBH-system the solid mixture was in the proportions of ideal liddicoatite end-member $[Ca(Li_2Al)Al_6(Si_6O_{18})(BO_3)_3(OH)_4]$, with identical H_3BO_3 and Li_2O in excess and a 6.8 mol/l saturated $CaCl_2$-solution. Solid to fluid proportions given to the Au-capsule were the same as in the NLABSH-experiment. The bulk composition of the

CASBH-experiment corresponds to the stoichiometric proportions of a hypothetic Ca-olenite end-member [$Ca(Al_3)Al_6(Si_6O_{18})(BO_3)_3O_4$], but with an excess of 300 mol % H_3BO_3, 150 mol % of $CaCl_2$ and a deficiency of 5 mol % SiO_2. 13.05 mg of the solid mixture were loaded together with 5.51 mg of a fluid containing 44 wt% $CaCl_2$ in solution to the gold capsule of the same dimensions. After loading, the capsules were welded shut. The capsules were placed into high-pressure cells consisting of a steel furnace with fired pyrophyllite and rock salt as pressure media. The pressure uncertainty of this assembly is approximately 1%, calibrated according to the quartz-coesite transition (Mirwald and Massonne 1980). Pressure was maintained constant within 50 MPa throughout the experiments. The temperature was monitored using a Ni-CrNi thermocouple, with an uncertainty estimated to be ±10°C. At the end of the experiments, the samples were quenched isobarically to below 200°C in less than 15 seconds and subsequently the pressure was released slowly. The capsules were then cleaned and reweighed to check for leakage. The solid products were removed, washed in pure water and prepared for powder X-ray diffraction, electron microprobe analyses and single-crystal Raman spectroscopy.

Powder X-ray diffraction (XRD)

Powder XRD analyses of solid products of the three experiments were performed with a fully automated STOE STADI P diffractometer at the GFZ Potsdam. It operated at 40 kV and 40 mA using Cu$K\alpha_1$ radiation and intensities were collected in the 2θ range 5 to 125° with a detector step size of 0.05°, a 2θ resolution of 0.01°, and counting times of 20 s per step. The powder XRD patterns were recorded in transmission mode (Bragg-Brentano geometry), using a MYTHEN-detector. An areal germanium-monochromator (Ge111) filters the Cu *K*β-radiation. Quantitative phase analysis, determination of the cell-dimensions and other structural parameters were refined using the GSAS software package for Rietveld refinement (Larson and Von Dreele 1987). The peak shape was defined as pseudo-Voigt with variable Gaussian and Lorentzian character. The peak full width at half height (FWHH) was varied as a function of

2θ using the parameters U, V, W of Caglioti et al. (1958); for the Lorentzian character the parameters X and Y were used. Background was fitted through a polynomial Chebyshev function, which is capable of modelling the diffuse background from the amorphous foil and glue used for sample preparation. Initial crystal structures were taken from the Inorganic Crystal Structure Database (ICSD, FIZ Karlsruhe). For tourmaline we used the structural input parameters of synthetic olenite (Marler et al. 2002), modified according to the EMP- and SIMS-determined site occupancies. Structural data for coesite and $AlBO_3$ were taken from Geisinger et al. (1987) and Vegas et al. (1977), respectively. The refinements were done in the following sequence: scale factor, background, zero-point correction, phase fractions, Caglioti W, lattice parameters, preferred orientation, atomic positions (except hydrogen), individual isotropic temperature deplacement factors, Caglioti U and V, Lorentz X and Y.

Electron microprobe analyses (EMPA)

The synthetic tourmaline composition (except hydrogen and lithium) was determined on a carbon-coated, polished grain mount by wavelength-dispersive X-ray spectroscopy (WDX) using a JEOL Hyperprobe JXA-8500F equipped with a thermal field emission gun and 5 spectrometers at the GFZ Potsdam. We used a low-beam current of 5 nA, accelerating voltages of 10 kV, and a beam diameter of 2-5 μm. A liquid nitrogen cold trap was used to reduce effects of hydrocarbon contamination. The following standards were used: Harvard 112566 (Schorl) for Si (Kα), Fe (Kα), Al (Kα) and B (Kα), wollastonite for Ca (Kα) and tugtupite for Na (Kα). The acquisition times were 40s for Na, B, Ca and Fe and 20s for Si and Al. The acquisition time to collect the background level on both sides of the corresponding peak was half of the peak acquisition time. Raw data were processed applying a φ(ρZ) correction scheme (CITZAF; Armstrong 1995). Measuring conditions resulted in analytical errors (1sigma) of ~0.5 % for Al, ~0.7 % for Si, ~0.1 % for Ca and Na and ~1 % for B. For formula calculations the EMP data were normalized to 18 cations at the Y, Z, T, and B sites. For the

two Li-bearing tourmalines, the Li_2O content (determined by SIMS) is included in the normalization scheme with all Li assigned to the Y site (see results and discussion for further information).

Secondary ion mass spectrometry (SIMS)

Lithium concentrations in synthetic tourmaline obtained from the NLASBH- and CLASBH-experiments were determined by SIMS analysis at the Helmholtz Center Potsdam, GFZ Potsdam, using a CAMECA 1280-HR instrument. Tourmaline crystals were embedded in two round 1-inch epoxi mounts, which were polished, ultrasonically cleaned in high-purity ethanol and coated with a 35 nm layer of high-purity gold. The mass resolution of the instrument was set to around 2500. Because the small crystal sizes of the analyzed tourmalines (Fig. 1) required small analytical spots, the primary $^{16}O^-$ ion beam was set to 0.04 nA and focussed to a ~ 3-4 μm diameter on the sample surface. Each analysis was preceded by a 120 second pre-sputter using a 20 μm raster to remove gold coating, suppress any surface contamination and establish stable sputter conditions. Secondary positively charged ions were extracted by means of a +10 kV potential with no offset voltage being applied.

The two isotopes of interest (^7Li, ^{28}Si) were measured dynamically, i.e. in peak-jumping mode using a single electron multiplier. A single analysis comprised 10 measurements of ^7Li and ^{28}Si each, with integration times of 4 s each. Dwell times between the peak jumps were 3 s (^7Li to ^{28}Si) and 5 s (^{28}Si to ^7Li), respectively. After preburn and before data acquisition, an automatic centering routine of the secondary beam was performed on the x and y axis, ensuring optimum alignment of the secondary ions into the mass spectrometer. Secondary ions were then energy filtered through a 50eV wide energy window by scanning of the extraction high voltage, followed by a 5eV shift relative to the value found. Finally, the mass calibration was checked

by scanning and tracking the ^{28}Si peak before analysis started. Thus, the total analysis time for a single point, including presputtering and centering routine, amounted to around 5 min.

The liddicoatite and elbaite crystals were analyzed 9 and 13 times, respectively. In order to control data quality and to correct for possible instrumental drift, the sample analyses were bracketed by repeated measurements of tourmaline reference materials 98144 (elbaite) characterized for its Li contents by Dyar et al. (2001). The in-run precision of the $^{7}Li/^{28}Si$ ratio was around 0.4 % (1 SD) for RM 98144 and 1.5 % (1 SD) for the two synthetic tourmalines. The relatively high analytical uncertainties reflect the low ^{7}Li counting rates due to the reduced primary beam. The repeatability of the $^{7}Li/^{28}Si$ ratio ranged between 5 % (RM 98144; 1 SD, n = 23), 12 % (elbaite, 1 SD) and 19 % (liddicoatite, 1 SD). The lower repeatibility of the experimental products as compared to RM 98144 is probably due to both lower ^{7}Li counting rates and possible sample heterogeneities. Data calibration and thus the determination of Li concentrations is based on the chemical composition and analytical data for RM 98144 and outlined in detail in Kutzschbach et al. (2017).

Raman spectroscopy

The Raman spectrum of Ca-olenitic tourmaline was recorded at room temperature using a HORIBA Jobin Yvon LabRAM HR800 UV-VIS spectrometer with a grating of 1800 grooves/mm located at the GFZ Potsdam. The 488 nm line of a coherent Ar^{+} laser model Innova 70-3 with a power of 220 mW was used for excitation, which corresponds to about 30 mW on the sample. By using an Olympus objective (100×) with a numerical aperture of 0.8, the spot sizes were 3-5 µm. Parallel polarized spectra have been acquired in *-y(zz)y* and *-y(xx)y* scattering geometries referring to Porto´s notation $k_i(E_iE_s)k_s$ with k_i and k_s being the wavevector and E_i and E_s the polarization of incident and scattered light, respetively. The axes *x,y, z* of the cartesian reference system are oriented such that *z* is parallel to the crystallographic **c**- axis of tourmaline applying the hexagonal setting. Tourmaline´s **a** axis is either parallel to *x* or *y* and

either orientation yields the same Raman spectrum (Watenphul et al., 2016).

Energy of the scattered photons was determined with a Peltier-cooled CCD detector at a resolution of about 1 cm^{-1}. Acquisition time for each spectrum was 30 s and 30 accumulations were performed for noise reduction. The region of the OH-stretching vibration was monitored between 3000 and 3800 cm^{-1}.

Raman spectra of elbaitic and liddcoatitic tourmalines have been recorded at the GFZ Potsdam using a HORIBA Jobin Yvon LabRAM HR800 VIS spectrometer with a grating of 1800 grooves/mm. For excitation the 473 nm line of a diode-pumped solid-state laser and a 10x Olympus objective was used. Measurements had to be performed on aggregates of randomly oriented crystals, because the crystals were simply too small and agglomerated to isolate a single crystal. Energy of the scattered photons was determined with a Peltier-cooled CCD detector at a resolution of about 1 cm^{-1}. Acquisition time for each spectrum was 60 s and 10 accumulations were performed for noise reduction. The Raman spectrum of sassolite (H_3BO_3) was recorded using the same instrument, but a 100x Olympus objective, 3s acquisition time and 10 accumulations.

Different combinations of acquisition time and number of accumulations for measurements of elbaitic tourmaline, liddicoatitic tourmaline and sassolite where chosen in order to achive a convenient compromise between total intensity, signal/noise ratio and measurement time. For data reduction, all spectra were fitted with the program PeakFit by Jandel Scientific after background subtraction using a cubic spline function. Band shapes were approximated with pseudo-Voigt functions and the criterion for the maximum number of functions included in the fit was $\Delta I \leq I \cdot 0.5$, where I is the integrated intensity of a particular band in counts and ΔI its uncertainty. Standard deviations (1 SD) for band position, integrated intensity (I) and full width at half maximum (FWHM) result from the fit itself. Error for the relative integrated intensity (I_{rel}) is calculated by error propagation. The r^2 value (goodness) of each individual fit is better then 0.999.

This is the peer-reviewed, final accepted version for American Mineralogist, published by the Mineralogical Society of America.
The published version is subject to change. Cite as Authors (Year) Title. American Mineralogist, in press.
DOI: https://doi.org/10.2138/am-2021-7758. http://www.minsocam.org/

RESULTS

Powder X-ray diffraction

Results from the powder XRD Rietveld refinement are summarized in Table 1. The quantitative phase analyses indicates that tourmaline was the main phase in all three synthesis experiments with contents between 60-90 wt %. Besides, coesite (10-24 wt%) has formed in all runs, whereas only in the CASBH-experiment $AlBO_3$ (16 wt%) has been found. Traces of sassolite (H_3BO_3) were also identified by the Raman measurements in the sample of the NLASBH-experiment (Fig. 2a).

The refined cell-dimensions of tourmaline from the three syntheses are the following: tourmaline from the NLASBH-experiment a = 15.681(1) Å, c = 7.054(1) Å, V = 1502.2(2) Å^3; tourmaline from the CLASBH-experiment a = 15.604(2) Å, c = 7.016(1) Å, V = 1479.4(4) Å^3; tourmaline from the CASBH-experiment a = 15.635(5) Å, c = 7.027(3) Å, V = 1488(1) Å^3. The cell-dimensions of the Li-bearing tourmalines are significantly smaller than those of natural elbaite and liddicoatite (e.g., Ertl et al. 2006; Lussier et al. 2011). Additionally, cell-dimensitions of the synthetic CASBH tourmaline are smaller than that of $^{[4]}$B-bearing natural olenite (Ertl et al. 1997). Applying the formula $^{[4]}B = (V - 1542) / (-29.242)$ for correlating the unit-cell volume with the tetrahedral B content after Ertl et al. (2018), yields 1.36(1) $^{[4]}$B pfu (NLASBH-experiment), 2.14(1) $^{[4]}$B pfu (CLASBH-experiment) and 1.85(4) $^{[4]}$B pfu (CASBH-experiment).

EMP and SIMS analyses

Tourmaline from the experiments are idiomorphic and large enough for reliable EMP and SIMS-analyses (Fig. 1a-c). Dimensions of tourmaline from the two Li-bearing experiments

This is the peer-reviewed, final accepted version for American Mineralogist, published by the Mineralogical Society of America.
The published version is subject to change. Cite as Authors (Year) Title. American Mineralogist, in press.
DOI: https://doi.org/10.2138/am-2021-7758. http://www.minsocam.org/

(up to 5 µm in diameter, 20 µm in length) are significantly smaller than those of the CASBH-experiment (up to 20 µm in diameter, 100 µm in length). From the SIMS- and EMPA-analyses, summarized in Table 2, we have no indication of any compositional zoning of the synthetic tourmaline.

For tourmaline of the NLASBH-system 13 individual SIMS-analyses resulted in 0.70(8) wt.% Li_2O (Table 2). We have no indication of Li at the X-site from the Raman-analyses (see below), therefore all Li is assigned to the Y-site. Together with the 30 individual EMP-analyses the calculated structural formula is:

$^{X}(Na_{0.74(5)}\square_{0.26(5)})^{Y}(Al_{2.55(1)}Li_{0.45(1)})^{Z}(Al_{5.94(7)}Si_{0.06(7)})^{T}(Si_{4.67(25)}B_{1.31(25)}Al_{0.01(3)})(BO_3)_3$

$^{V+W}(OH_{3.41(24)}O_{0.59(24)})$.

Thus, the synthetic tourmaline is best described as a solid solution between the end member "□-Li-O root name" (Henry et al. 2011) and „Na-Al-Al-B root name" (Henry et al. 2011, Schreyer et al. 2000). We decided to avoid using these rather unusual designations to help the reader to better comprehend the paper and instead use the term „elbaitic tourmaline" as similar to the NLASBH tourmaline, Na and Li are found at the X and Y sites in elbaite, respectively.

For tourmaline of the CLASBH-system 9 SIMS-analyses resulted in 0.58(11) wt.% Li_2O (Table 2). Assigning all Li to the Y site, the combined SIMS- and 20 EMP-analyses resulted in the structural formula:

$^{X}(Ca_{0.80(3)}\square_{0.20(3)})^{Y}(Al_{2.63(0)}Li_{0.37(0)})^{Z}(Al_{5.83(9)}Si_{0.17(9)})^{T}(Si_{3.80(18)}B_{2.20(19)}Al_{0.01(3)})(BO_3)_3$

$^{V+W}(OH_{3.17(12)}O_{0.83(12)})$.

Thus, the tourmaline seems to represent a solid solution of the end members "□-Li-O root name" (Henry et al. 2011) and the hypothetical end-member $CaAl_3Al_6(B_3Si_3O_{18})(BO_3)_3(OH)_3O$. Again for the sake of readability, we decided to use the more generic term "liddicoatitic tourmaline" for this synthetic tourmaline as like liddicoatite it contains both Ca at the X site and Li at the Y site.

An average of 14 EMP-analyses of tourmaline from the CASBH-experiment gave the structural formula:

This is the peer-reviewed, final accepted version for American Mineralogist, published by the Mineralogical Society of America.
The published version is subject to change. Cite as Authors (Year) Title. American Mineralogist, in press.
DOI: https://doi.org/10.2138/am-2021-7758. http://www.minsocam.org/

$^{X}(Ca_{0.39(8)}\ \square_{0.61(8)})^{Y}(Al._{3.00(0)})^{Al.}Al_{5.86(8)}Si_{0.14(8)})^{T}(Si_{4.43(25)}B_{1.57(25)}Al_{0.00(1)})(BO_3)_3$

$^{V+W}(OH_{2.65(10)}O_{1.35(10)})$,

which is a solid solution between the hypothetical end members $\square Al_3Al_6(B_2Si_4O_{18})(BO_3)_3(OH)_4$ and $CaAl_3Al_6(Si_6O_{18})(BO_3)_3O_4$. Due to the latter being a variety of olenite with Ca substituting for Na at the X site, we term this hypthetical end member "Ca-olenite" and thus the synthetic tourmaline from the CASBH experiment "Ca-olenitic tourmaline".

All three tourmalines show a small, but significant amount of Si at the octahedral Z site, which has already been observed for other synthetic tourmaline from high-pressure syntheses (Schreyer et al. 2000; Wunder et al. 2015).

Raman spectra between 3000-3800 cm^{-1}

Raman spectra have been recorded between 3000-3800 cm^{-1} corresponding to the frequency region of the O-H stretching vibration. Individual spectra of the three synthetic tourmalines are deconvoluted using 6-8 bands (Fig. 2), which in each spectrum have been arbitrarily numbered ν_1- ν_8 with ν_1 denoting the band at the lowest wavenumber. On the basis of their location, FWHM and relative integrated intensity (data compiled in Table 3) the Raman bands can be roughly separated in two groups. As opposed to the highest frequency bands (> 3550 cm^{-1}), which are generally of lower intensity and appear rather sharp, Raman bands in the lower frequency region (<3550 cm^{-1}) are of higher intensity and become increasingly broader with decreasing wavenumber. Whereas some bands are recognized in all three Raman spectra (e.g. band between 3451-3469 cm^{-1} and 3564-3584 cm^{-1}), additional similarities are found comparing either lithian tourmalines (e.g. band between 3601-3623 cm^{-1} in elbaitic and liddicoatitic tourmaline) or calcic tourmalines (e.g. band between 3423-3430 cm^{-1} and 3528-3533 in liddicoatitic and Ca-olenitic tourmalines). However, in the case where Raman bands

have been identified at roughly the same position, their integrated intensity may differ significantly among the three tourmalines (Fig. 2, Table 3).

In the Raman spectrum of elbaitic tourmaline two bands appear at 3171 and 3250 cm^{-1}, which have not been found in any of the other samples (Fig. 2, top). By comparing their location and intensity ratio to the Raman spectra of sassolite, it became evident that these bands stem from solid H_3BO_3, which is interpreted as a quench phase. The absence of sassolite in the other experimental run products is due to their having been washed with distilled water after opening the capsule, which effectively removed the highly soluble H_3BO_3. Hence, bands at 3171 and 3250 cm^{-1} in elbaitic tourmaline are excluded in the following discussion.

DISCUSSION

Raman band assignments

The Raman spectra of all synthetic tourmaline show a multitude of bands in the OH-stretching frequency region (Fig. 2). A part of the diversity arises from the two different oxygen sites in tourmaline (O1 and O3) where protonation occurs (Fig. 3). Due to pronounced hydrogen bridge bonding between the protonated O3 site and the acceptor oxygen O5 (Gatta et al. 2014, see also Fig. 3), O3-H bands always occur at lower wavenumbers (Fig. 2), roughly corresponding to the lower frequency region (< 3550 cm^{-1}) defined in the results section. The strength of the hydrogen O3-H…O5 bridge bonding is affected by the T-site occupancy, with $^{[4]}B^{3+}$ instead of $^{[4]}Si^{4+}$ increasing the hydrogen bridge bonding and hence causing a low-wavenumber shift of the O3-H bands. This effect is even more pronounced if the X site is left vacant (Kutzschbach et al. 2016; Fig. 3). The X-site occupancy also influences O1-H stretching frequencies, in that cations of higher valence and larger size cause a shift of the associated O1-H bands to higher frequencies (Berryman et al. 2015).

Further complexity is added because the O1-H and O3-H sites are surrounded by cation triplets, namely YYY and YZZ (Fig. 3). While in the synthetic tourmalines under

investigations, Al is the only relavant Z occupant (>97 % Al on Z), a significant portion (12-15%) of the Al on the Y site is substituted by Li. Depending on the total positive charge of the cation triplets, the corresponding Raman bands are shifted, with the higher charged triplets being located at lower wavenumber. Based on these considerations a consistent Raman band assigments is established, which is compiled in Table 3 and Fig. 2.

Verifying band assignments by calculating site occupancies from Raman spectra

In order to test the correctness of the cation configurations assigned to the O3-H and O1-H bands, cation occupancies at X, Y and T sites are calculated applying the procedure described in Kutzschbach et al. (2017b). The calculation involves transferring the relative integrated intensities into probabilities for the occurrence of a certain cation arrangement by normalizing the relative integrated intensities of individual O3-H and O1-H bands to the sum of relative intensities of all bands belonging to either O3-H or O1-H stretching vibrations. This internal normalization scheme has the advantage that the results are independent of the analytical conditions (e.g., laser power, acquisition time, accumulations). Still, a bias might be caused by the polarization of the laser, but this will be addressed later. To derive the probability (P) of the configuration $^{Z}(AlAl)^{Y}(Li)^{T}(B,Si)^{X}Na$ around O3-H in elbaitic tourmaline for example, the relative integrated intensity of the according band ν_2 is divided by the summed relative integrated intensities of ν_1, ν_2, ν_3, ν_4 and ν_6 to obtain the probability with $P_{\nu2} = 0.475$. The cation occupancy at a specific site (in atoms pfu) is then calculated by multiplying the sum of the probability (P) weighted partial cluster occupancies (x) by the site multiplicity (M). The partial cluster occupancies for the configuration $^{Z}(AlAl)^{Y}(Li)^{T}(B,Si)$ are for example, $x^{Y}Li = 1$, $x^{Z}Al = 1$ and $x^{T}B = x^{T}Si = 0.5$； the partial cluster occupancy for Li in $^{X}\square^{Y}(LiAlAl)$ is 0.33. Finally, the amount of B at the T site based on O3-H vibrations is calculated with:

$$^{T}B\ (pfu) = M_T \times [(x^{T}B)_{\nu1} \times P_{\nu1} + (x^{T}B)_{\nu2} \times P_{\nu2} + (x^{T}B)_{\nu3} \times P_{\nu3} + (x^{T}B)_{\nu4} \times P_{\nu4} + (x^{T}B)_{\nu6} \times P_{\nu6}]$$

This is the peer-reviewed, final accepted version for American Mineralogist, published by the Mineralogical Society of America.
The published version is subject to change. Cite as Authors (Year) Title. American Mineralogist, in press.
DOI: https://doi.org/10.2138/am-2021-7758. http://www.minsocam.org/

$$= 6 \times [(0.5 \times 0.024 + 0.5 \times 0.475 + 0 \times 0.125 + 0 \times 0.331 + 0 \times 0.045]$$

$$= 1.497 \approx 1.50$$

X- and Y-site occupancies are calculated by analogous equations (see also additional formulae presented in Kutzschbach et al. 2017b).

A simplified calculation scheme has been applied in cases where relevant bands are missed due to superposition of more intense bands. An example is the calculation of the ^{X}Na content in elbaitic tourmaline based on O1-H vibrations. Here, the relative integrated intensity of the band related to the configuration $^{X}Na^{Y}$(AlAlAl) would be needed. However, this band could not be detected as it is probably superimposed by band ν_6 referring to the ^{Z}(AlAl)^{Y}(Li)^{T}(Si)^{X}Na configuration around the O3-H bond. Hence, the ^{X}Na content is estimated by calculating the ratio $I_{rel}(\nu_8) / [I_{rel}(\nu_7) + I_{rel}(\nu_8)] = 0.67\ ^{X}$Na (pfu) , with ν_8 and ν_7 referring to the $^{X}Na^{Y}$(LiAlAl) and $^{X}\square^{Y}$(LiAlAl) bands respectively. Analogue cases are labelled in Table 4.

Special care has to be taken, because V and W sites are partially deprotonated and hydrogen atoms might not be equally distributed among different cation arrangements. It is likely that a hydrogen will prefer to attach to an oxygen that is surrounded by the lower positive charge, i.e., has the least incident positive valence. For example, an O3-H band is more likely to appear within a configuration including a vacant X site and B at the T site compared to configuration with an occupied X site and tetrahedral Si only. This might influence to some extent the cation occupancies derived from the Raman band assignment.

Calculating Li concentrations from O3-H vibrations is difficult due to the low Li concentrations which complicate the unambiguous detection of bands involving ^{Y}(Li)^{Z}(AlAl) triplets. These bands are most likely hidden underneath other more intense bands. An example would be the intense band ^{Z}(AlAl)^{Y}(Al)^{T}(Si,B)^{X}(Na) in elbaitic tourmaline (ν_2), which is likely superimposing the low intensity band ^{Z}(AlAl)^{Y}(Li)^{T}(Si,B)$^{X}\square$. Conversely, the influence of

bands related to Li on Y site in YZZ is negligible for the other cation assignments derived from the O3-H vibrations.

Calculating ^{X}Ca contents from O1-H bands in liddicoatitic tourmaline is not possible as no O1-H band related to Ca at the X site is detected. This might be because the highly positively charged Ca^{2+} deprotonates the O1 position, an effect that has also been found in other synthetic Ca-bearing tourmalines such as magnesio-lucchesiite (Berryman et al. 2015). However, in Ca-olenite, Ca at the X site is obviously stable together with an O1-H group.

All cation occupancies, which have been calculated from the Raman specta are compiled in Table 4 and Fig. 4 and are, within errors, in agreement to the EMP/SIMS measurements and the results obtained by powder-XRD, thus supporting the choice of Raman band assignments.

Effect of O-H bond orientation on site occupancies derived from Raman spectra

Because Raman spectra have been obtained using polarized light, the crystallographic orientation of the O-H vector has to be considered. Previous spectroscopic studies agree that the O1-H1 vector is aligned parallel to the crystallographic **c**- axis or is displaced off-axis at an angle O1-H1 ∠ [0001] ~15.6(5)° (Gatta et al. 2014 and references therein). The exact angle is thought to be variable among different tourmaline species responding to the occupation of the YYY cation triplet, with a more pronounced displacement for YYY triplets that show a more asymmetrical charge distribution (Gonzalez-Carreño et al. 1988; Gatta et al. 2014). For the tourmaline species investigated in this study only ^{Y}(AlAlAl) or ^{Y}(LiAlAl) are present, with the latter being expected to have a greater O1-H1 ∠ [0001] angle.

Consequently, in Raman spectra, which have been acquired in *-y(zz)y* scattering geometry, the probability of configurations involving ^{Y}(LiAlAl) configurations and cation occupancies deduced from them might be underestimated. In principle this would only be relevant for the rossmanite spectra of Kutzschbach et al. (2017b). Olenite and Ca-olenitic tourmaline do not contain Li and hence only ^{Y}(AlAlAl) configurations are present and the other

Li-bearing tourmalines (elbaitic and liddocoatitic tourmaline) were measured as aggregates of randomly oriented crystals and hence the resulting probabilities and cation configurations are independent of orientation of the O1-H1 vector. However, as shown in Fig. 4 the cation occupancies derived from rossmanite are in very good agreement with the EMP/SIMS derived data and it is therefore reasonable to exclude a significant effect of the orientation of O1-H1 groups on the site occupancies calculated from the Raman spectra in this study.

For the O3-H3 stretching vibrations an effect of orientation is also excluded, as it has been shown that the angle O3-H3 $\angle$ [0001] is small and rather constant across different tourmaline species [e.g., ~3.4° in oxy-dravite (Gatta et al. 2014); 1.3° in fluor-buergerite (Tippe and Hamilton 1971); and 5.4° in fluor-elbaite (Gatta et al. 2012)].

Given that the orientation of O-H groups is negligible for the tourmaline species under investigation, it makes no difference whether site occupancies have been obtained from randomly oriented aggregates (liddicoatitic and elbaitic tourmaline) or oriented single crystals (Ca-olenitic tourmaline, olenite, rossmanite). This is also supported by the constant intensity ratios for *-y(zz)y* versus *-y(xx)y* scattering geometries of all O3-H3 bands of the Ca-olenitic tourmaline (Fig. 2c, Fig. 5, Table 5).

Alternative band assignment based on Watenphul et al. (2016)

The approach that has been used for the assignment of the Raman bands relies on the idea that each of the three O3-H3 groups within the unit cell produces a distinct Raman band. Considering for example end-member elbaite $Na(Li_{1.5}Al_{1.5})Al_6Si_6O_{18}(BO_3)_3(OH)_4$ with Al-only at the Z site and mixed Li and Al occupancy at the Y site, two distinct bands would appear for each of the possible YZZ triplets surrounding the O3-H3 group, one for the LiAlAl configuration and one for the AlAlAl configuration. This assignment model was first used by Gonzalez-Carreño et al. (1988) and has been successfully adopted by many other spectroscopists and crystallographers over the past decades to link vibrational spectra of

tourmaline to its crystal chemistry (e.g. Castañeda 2000; Veličkov 2002; Bosi et al. 2012; Bosi et al. 2015 Skogby et al. 2012; Fantini et al. 2014; Berryman et al. 2015; Kutzschbach et al. 2016; Kutzschbach et al. 2017b).

Recently, Watenphul et al. (2016) introduced a new way to assign Raman spectra of tourmaline based on group theory and the fundamental work of Chang and Mitra (1971). They argue that the H3 cations (from the O3-H3 groups) in tourmalines occupy the 3b Wyckoff position in space group R3m and therefore all three H3 cations participate in a single phonon mode producing a discinct band in the vibrational spectrum. Hence, all atomic sorroundings of all three O3-H3 groups, i.e. YZZ-YZZ-YZZ units, have to be considered when analyzing the effect of chemistry. For the case of elbaite this would lead to a maximum of 4 possible bands corresponding to the AlAlAl-AlAlAl-AlAlAl, LiAlAl-AlAlAl-AlAlAl, LiAlAl-LiAlAl-AlAlAl and LiAlAl-LiAlAl-LiAlAl configurations. Watenphul et al. (2016) were able to apply this concept to a large number of tourmaline chemistries, e.g. natural F-liddicoatite whose spectra contains all of the four "elbaite" bands mentioned above (see Fig. 5f in Watenphul et al. 2016). A consistent band assignment according to the approach of Watenphul et al. (2016)

After a thorough review of an earlier version of the Manuscript (see acknowledgments), we became aware of this problem and could establish a consistent band assignment based on the approach of Watenphul et al. (2016) in Table 5. For the sake of completeness, Table 5 also includes a re-assignment of two spectra of synthetic $^{[4]}$B-bearing olenite and rossmanitic tourmaline, that have been published earlier in Kutzschbach et al. (2016) and Kutzschbach et al. (2017b), respectively. A good agreement is obtained for most assignments in the synthetic high-$^{[4]}$B tourmalines and the natural $^{[4]}$B-free, Al-rich tourmalines in Watenphul et al. (2016), e.g. for the (□-AlAlAl-AlAlAl-AlAlAl)$^{(Si)}$ configuration which has been ascribed to a band at 3455 cm^{-1} in natural olenite in Watenphul et al. (2016, their Table 3) and to bands between 3451-3469 cm^{-1} in the five synthetic tourmalines (Table 6). However, for the synthetic elbaitic tourmaline, the O1-H1 bands occur at 20-60 cm^{-1} lower wavenumbers compared to the results

of Watenphul et al. (2016). This might be caused by the high amount of trivalent B substituting for Si at the tetrahedral site, which increases the negative charge at O4 and O5 in the T_6O_{18} ring, lowers the effective positive charge of the X-site cation and hence enables longer O1-H1 bands, ultimately appearing at lower wavenumbers as compared to $^{[4]}$B absent configurations (see also Fig. 3).

Calculation of tetrahedral boron content from Raman spectra

Evaluation of the Raman spectra shows that the assignment of Raman bands and subsequent deduction of tourmaline composition is not trivial due to (1) the superposition of different cation configurations leading to an identical Raman shift (2) variations in frequency shifts of identical configurations in tourmalines with different composition (3) different off-axis displacements of O-H vectors in the case oriented single crystal measurements and (4) the multitude of major elements that are incorporated at X,Y,Z and T sites in natural tourmaline (e.g., Henry et al. 2011). Another complication is the existence of the two competing ways to assign Raman bands. It has been mentioned earlier, that the biggest difference between the Gonzalez-Carreño et al. (1988) and the Watenphul et al. (2016) approach is the group-theoretical view of the structural units. However, both models agree on the position of the bands related to tetrahedral boron and share a common crystal chemical explanation for their occurrence, i.e. a shift to lower wavenumbers caused by increased strength of O3-H…O5 hydrogen bonding due to the lower charged B^{3+} substituting for Si^{4+} which is neighbouring the O5.

This is the reason that regardless of the assignment model used a solid linear trend is obtained between the T-site boron derived from EMPA and the summed relative intergrated intensity of all bands associated with tetrahedral boron, i.e., bands in the frequency region between 3300-3430 cm^{-1} (Fig. 6). The correlation is described by the following regression equation:

This is the peer-reviewed, final accepted version for American Mineralogist, published by the Mineralogical Society of America.
The published version is subject to change. Cite as Authors (Year) Title. American Mineralogist, in press.
DOI: https://doi.org/10.2138/am-2021-7758. http://www.minsocam.org/

(1) $^{[4]}B\ [pfu] = 0.030(3) \cdot \sum_{\upsilon=3300\ cm^{-1}}^{3430\ cm^{-1}} I_{rel}\ (\nu)[\%]$,

with $^{[4]}$B being the tetrahedrally-coordinated boron content per formula unit, ν the wavenumber of the Raman band and I_{rel} its relative integrated intensity in percent. This equation represents a simplified but accurate way to calculate the tetrahedral boron content from intensities of OH-stretching bands. It does not require in depth knowledge of vibrational spectroscopy, group theory and band assignments and works equally well for powders and single crystals. For the latter, to obtain the most accurate results, the scattering geometry must be chosen in a way that the polarization of incidient and scattered light are parallel to the crystallographic **c**-axis, i.e. -*y(zz)y* applying Porto´s notation (an orientation which is recognized by yielding maximum intensity upon rotation of the sample about the *y* axis of the reference coordinate system; see section "Raman spectroscopy"). This is due to the fact that in equation (1) the Raman bands related to tetrahedral B are normalized to the intensity of O1-H1 *and* O3-H3 bands and not to the summed intensity of O3-H3 bands only as it has been described in the discussion "Verifying band assignments by calculating site occupancies from Raman spectra". However, for single crystal spectra obtained in -*y(zz)y* scattering geometry and for spectra obtained from randomly oriented powdered samples the summed relative intensity of O1-H1 bands is negligible (< 8 %) and hence for the sake of simplicity they can be included in the normalization procedure. Only for -*y(xx)y* scattering geometries tetrahedral boron contents are likely to be underestimated due to the decreasing intensity ratio of O3-H3 and O1-H1 bands (see Raman spectrum of Ca-olentitic tourmaline obtained in -*y(xx)y* scattering geometry; Fig. 5, Table 5)

As distinct from occupancies at Y, Z and X sites equation (1) is expected to also hold for natural tourmalines without any corrections because Raman bands associated with tetrahdral boron occur in the lowest frequency region and here interferences from other cation configuration are absent. This conclusion is supported when the tetrahedral boron content of natural excess boron-bearing tourmaline from the Koralpe is calculated using equation (1). The EMPA derived value of 0.67(12) $^{[4]}$B (Kutzschbach et al. 2016) is in perfect agreement with

the result obtained by Raman spectroscopy [0.66(13) $^{[4]}$B pfu]. This example also illustrates that the accuracy and precision obtained by the Raman-method are as good as for the EMPA data. However, the measurement of light elements such as B by electron microprobe is generally challenging (e.g., Bastin and Heijligers 1990) and requires besides a careful sample preparation (e.g., perfectly polished surface, equal thickness of graphite coating for reference material and sample) and data evaluation method, the availability of suitable reference materials (e.g., Harvard tourmalines, Dyar et al. 2001) and multi-layer monochromator crystals (e.g., LDEB for JEOL or PC2 for CAMECA electron microprobes). In contrast, the Raman spectra of tourmaline can be acquired in a short time span (<< 1 hour) and without any special sample preparation making the analyses of tetrahedral boron in tourmaline accessible for a wide-range of laboratories, which lack advanced electron microprobes and experienced analytical personel.

If powder XRD is used for the quantification of $^{[4]}$B by applying the unit cell volumes, the tetrahedral boron content overlaps within one 1 SD with the EMPA and Raman data (Table 4). The good agreement can be attributed to the homogeneity of the tourmalines under investigation in this study and larger deviations between results from powder XRD and EMPA/Raman are likely for zoned crystals.

Despite the strength of the established Raman correlation (Fig. 6), deviations could appear due to tetrahedral boron that is associated with Mg substituting for Al in YZZ triplets coordinating O3 sites, as this would shift the relevant Raman band to higher frequencies then observed for tourmalines with Al-only at Y and Z (e.g., Gonzalez-Carreño et al. 1988; Fantini et al. 2014; Watenphul et al. 2016). However, natural Mg-tourmalines with excess boron are rare and in fact only one example of $^{[4]}$B-bearing dravite has been reported (~0.26 $^{[4]}$B pfu, Marschall et al. 2004).

Another potential pitfall is the incorporation of trivalent Al at the T site as this might cause a similar low wavenumber shift as observed for tetrahedral boron. To date, $^{[4]}Al^{3+}$ contents of up to 0.85 pfu $^{[4]}Al^{3+}$ have been reported (Nishio-Hamane et al. 2014), but such high

tetrahedral Al contents are restricted to Mg- and/or Fe^{2+}-rich compositions (Ertl et al. 2018). In Al-rich tourmalines, which are the most relevant host for tetrahedral boron, $^{[4]}Al^{3+}$ does not exceed 0.27 pfu (Ertl et al. 2007). If intensity related to tetrahedral Al would contribute to the frequency region 3300-3430 cm^{-1}, the tetrahedral boron content calculated by equation (1) would be overestimated. However, this seems not to be the case given that there is perfect agreement between the EMPA and Raman derived $^{[4]}$B-values of the Koralpe tourmaline, which also contains 0.27 $^{[4]}$Al. This might be explained by the larger size of $^{[4]}Al^{3+}$ compared to $^{[4]}B^{3+}$ (0.53 vs 0.25; Shannon 1976), which leads to a less pronounced Raman shift leaving the low frequency region free of interference.

Li-site occupancy

Applying the lattice-strain theory (Blundy and Wood 2003) on experimental data of trace-element partitioning between tourmaline and melt, van Hinsberg (2011) argued that beside its incorporation at the Y site, Li might also occur at the X site in tourmaline. This is supported by a study on synthetic rossmanitic tourmaline, in which evidence is provided that a significant portion of Li occurs at the X site (Kutzschbach et al. 2017b). Here, Raman bands associated with ^{X}Li have been found at 3648 cm^{-1} [$^{X}Li^{Y}$(AlAlAl) configuration around O1-H] and 3706 cm^{-1} [$^{X}Li^{Y}$(LiAlAl) configuration around O1-H], with the former being of higher intensity due to the higher Al content at the Y-site. While no band at 3706 cm^{-1} has been detected in the liddicoatitic and elbaitic tourmalines, bands in the proximity of 3648 cm^{-1} are present (Fig. 2, Table 3). However, these bands have been assigned to configurations, which do not involve Li at the X site [band $^{X}Na^{Y}$(LiAlAl) at 3657 cm^{-1} in elbaitic and band $^{X}\square^{Y}$(LiAlAl) at 3648 cm^{-1} in liddicoatitic tourmaline]. Variations of some 10 cm^{-1} can occur for a particular cation configuration across different tourmalines, so that the location of ^{X}Li bands observed in rossmanitic tourmaline might not necessarily be constant. Even if so, superposition of the other Raman bands in the lithian tourmalines prevents an unambiguous assignment of Li at the X site

in liddicoatitic and elbaitic tourmalines, which can neither be confirmed nor excluded on the basis of their Raman spectra.

IMPLICATIONS

Geologic mass-transfer processes are effectively traceable by deciphering the boron isotope record of tourmaline imprinted by its host fluid. Recently, it has been shown that the associated isotope fractionation correlates with the amount of tetrahedral boron in tourmaline (Kutzschbach et al. 2017a). Boron isotope studies should therefore include estimates of tourmaline´s T site occupancy. In this study we demonstrate that Raman spectroscopy provides a fast and easy-to-use tool for the quantification of tetrahedral boron in tourmaline. We could show, that for the determination of the $^{[4]}$B-contents in tourmaline EMPA and Raman-spectroscopy yield consistent results. We also demonstrate that Raman spectroscopy offers a reliable method for a fast, non-destructive chemical characterization and thus classification of precious tourmalines, supporting gemological appraisals.

In this study for the first time syntheses of elbaitic, liddicoatitic and Ca-olentic tourmaline from seed-free starting materials are decribed. In contrast to natural tourmaline which are nearly always solid solutions of multiple components, the tourmaline presented here were synthesized in chemically simple systems. Chemical and physical properties of end-member tourmaline are prerequisite to calculate for example phase equilibria that involve tourmaline and cannot be provided from chemically complex natural tourmaline. The advantages of using synthetic near-endmember tourmalines in constraining thermodynamic parameters has already been demonstrated by Berryman et al. (2019), who successfully deduced the compressibility of Mg-Al tourmalines. The newly synthesized tourmalines enable an extension of similar datasets especially with respect to lithian tourmalines, which commonly occur in evolved granites and pegmatites.

The assignment of the Raman spectra also has important crystal-chemical implications.

This is the peer-reviewed, final accepted version for American Mineralogist, published by the Mineralogical Society of America.
The published version is subject to change. Cite as Authors (Year) Title. American Mineralogist, in press.
DOI: https://doi.org/10.2138/am-2021-7758. http://www.minsocam.org/

This includes the stability of ^{Y}(AlAlAl) triplets sourrounding protonated O1 sites, a configuration which had thought to be unstable (Hawthorne 2002). Moreover, in the Ca-olenitic tourmaline, Ca at the X site does not lead to deprotonation at the O1 oxygen, which is otherwise a common phenomena (Berryman et al. 2015). Although these special crystal-chemical configurations seem to be a unique feature of tetrahedral B-rich tourmalines, the newly synthesized tourmalines further underline the immense chemical flexibility of the tourmaline structure, which is still not yet fully explored.

ACKNOWLEDGEMENTS

We thank H.-P. Nabein for collecting the XRD spectra and U. Dittmann for the preparation of samples for EMPA. O. Appelt is acknowledged for her support during EMP and I.Schäpan for help with REM imaging. Thanks to D. R. Baker for editorial handling of the manuscript and A. Ertl, E. Grew and B. Mihailova for their thorough reviews. The latter was particularly valuable for improving the manuscript by helping to establish a consistent band assigment according to the Watenphul et al. (2016) approach. This study was supported by funding from the Deutsche Forschungsgemeinschaft granted to G.F. and W.H. (Fr 557/31-1; HE 2015/16-1).

REFERENCES CITED

Armstrong, J.T. (1995) CITZAF: a package of correction programs for the quantitative electron microbeam X-ray-analysis of thick polished materials, thin films, and particles. Microbeam Analysis, 4, 177-200.

Bast, R., Scherer, E.E., Mezger, K., Austrheim, A., Ludwig, T., Marschall, H.R., Putnis, A., and Löwen, K. (2014) Boron isotopes in tourmaline as a tracer of metasomatic processes in the Bamble sector of Southern Norway. Contributions to Mineralogy and Petrology, 168 (4), 1-21.

Bastin, G.F., and Heijligers, H.J.M. (1990) Quantitative electron-probe microanalysis of ultralight elements (boron-oxygen). Scanning, 12, 225-236.

Berryman, E.J., Wunder, B., Wirth, R., Rhede, D., Schettler, G., Franz, G., and Heinrich, W. (2015) Influence of the X-site composition on tourmaline´s crystal structure:

investigation of synthetic K-dravite, dravite, oxy-uvite, and magnesio-foitite using SREF and Raman spectroscopy. Physics and Chemistry of Minerals, 43, 83-102.

Berryman, E.J., Kutzschbach, M., Trumbull, R.B., Meixner, A., van Hinsberg, V., Kasemann, S.A., and Franz, G. (2017) Tourmaline as a petrogenetic indicator in the Pfitsch Formation, Western Tauern Window, Eastern Alps. Lithos, 284-285, 138-155.

Berryman, E.J., Zhang, D., Wunder, B., and Duffy, T.S. (2019) Compressibility of synthetic Mg-Al tourmalines to 60 GPa. American Mineralogist, 104, 1005-1015.

Blundy, J., and Wood, B. (2003) Partitioning of trace elements between crystals and melts. Earth and Planetary Science Letters, 210, 383-397.

Bosi, F., Skogby, H., Agrosì, G., and Scandale, E. (2012) Tsilaisite, $NaMn_3Al_6(Si_6O_{18})(BO_3)_3(OH)_3OH$, a new mineral species of the tourmaline supergroup from Grotta d´Oggi, San Pietro in Campo, island of Elba, Italy. American Mineralogist, 97, 989-994.

Bosi, F., Skogby, H., Lazor, P., and Reznitskii, L. (2015) Atomic arrangements around the O3 site in Al- and Cr-rich oxy-tourmalines: a combined EMP, SREF, FTIR and Raman study. Physics and Chemistry of Minerals, 42, 441-453.

Castañeda, C., Oliveira, E.F., Gomes, N., and Soares, A.C.P. (2000) Infrared study of OH sites in tourmaline from the elbaite-schorl series. American Mineralogist, 85, 1503-1507.

Caglioti, G., Paoletti, A., and Ricci, F.P. (1958) Choice of collimators for crystal spectrometer for neutron diffraction. Nuclear Instruments, 3, 223-228.

Chang, I.F., and Mitra, S.S. (1971) Long wavelength optical phonons in mixed crystals. Advances in Physics, 20, 359-404.

Codeço, M.S., Weis, P., Trumbull, R.B., Glodny, J., Wiedenbeck, M., and Romer, R.L. (2019) Boron isotope muscovite-tourmaline geothermometry indicates fluid cooling during magmatic-hydrothermal W-Sn ore formation. Economic Geology, 114, 153-163.

Dyar, M.D., Wiedenbeck, M., Robertson, D., Cross, L.R., Delaney, J.S., Ferguson, K., Francis, C.A., Grew, E.S., Guidotti, C.V., Hervig, R.L., Hughes, J.M., Husler, J., Leeman, W., McGuire, A.V., Rhede, D., Rothe, H., Paul, R.L., Richards, I., and Yates, M. (2001) Reference Minerals for the Microanalysis of Light Elements. Geostandard Newsletter, 25 (2-3), 441-463.

Ertl, A., Pertlik, F., and Bernhardt, H.J. (1997) Investigations on olenite with excess boron from the Koralpe, Styria, Austria. Anzeiger der Österreichischen Akademie der Wissenschaften, Abteilung I, 124, 3-10.

Ertl, A., Hughes, J.M, Prowatke, S., Ludwig, T., Brandstätter, F., Körner, W., and Dyar, M.D. (2007) Tetrahedrally coordinated boron in Li-bearing olenite from "Mushroom" tourmaline from Momeik, Myanmar. Canadian Mineralogist, 45(4), 891-899.

Ertl, A., Hughes, J.M., Prowatke, S., Ludwig, T., Prasad, P.S.R., Brandstätter, F., Körner, W., Schuster, R., Pertlik, F., and Marschall, H. (2006) Tetrahedrally coordinated boron in tourmalines from liddicoatite-elbaite series from Madagascar: Structure, chemistry, and infrared spectroscopic studies. American Mineralogist, 91, 1847-1856.

Ertl, A., Henry, D.J., and Tillmanns, E. (2018) Tetrahedral substitutions in tourmaline: a review. European Journal of Mineralogy, 30, 465-470.

Fantini, C., Tavares, M.C., Krambrock, K., Moreira, R.L., and Righi, A. (2014) Raman and infrared study of hydroxyl sites in natural uvite, fluor-uvite, magnesio-foitite, dravite and elbaite tourmalines. Physics and Chemistry of Minerals, 41(4), 247-254.

Gatta, G.D., Bosi, F., McIntyre, G.J., and Skogby, H. (2014) First accurate location of two proton sites in tourmaline: A single-crystal neutron diffraction study of oxy-dravite. Mineralogical Magazine, 78, 681-692.

Gatta, G.D., Danisi, R.M., Adamo, I., Meven, M., and Diella, V. (2012) A single-crystal neutron and X-ray diffraction study of elbaite. Physics and Chemistry of Minerals, 39, 577-588.

Geisinger, K.L., Spackman, M.A., and Gibbs, G.V. (1987) Exploration of structure, electron density distribution, and bonding in coesite with fourier and pseudoatom refinement methods using single-crystal X-ray diffraction. Physics and Chemistry of Minerals, 91, 3237-3244.

Gonzalez-Carreño, T., Fernandez, M., and Sanz, J. (1988): Infrared and electron microprobe analysis of tourmalines. Physics and Chemistry of Minerals, 15(5), 452-460.

Guo, S., Zhao, K., John, T., Tang, P., Chen, Y., and Su, B. (2019) Metasomatic flow of metacarbonate-derived fluids carrying irotopically heavy boron in continental subduction zones: Insights from tourmaline-bearing ultra-high pressure eclogites and veins (Dabie terrane, eastern China). Geochimica et Cosmochimica Acta, 253, 159-200.

Hawthorne, F.C. (2002) Bond-valence constraints on the chemical composition of tourmaline. Canadian Mineralogist, 40, 789-797.

Henry, D.J., and Dutrow, B.L. (1996) Metamorphic tourmaline and its petrologic applications. Reviews in Mineralogy, 33(1), 503-557.

Henry, D.J., Novák, M., Hawthorne, F.C., Ertl, A., Dutrow, B.L., Uher, P., and Pezzotta, F. (2011) Nomenclature of the tourmaline-supergroup minerals. American Mineralogist, 96, 895-913.

Kowalski, P.M., Wunder, B., and Jahn, S. (2013) Ab initio prediction of equilibrium boron isotope fractionation between minerals and aqueous fludis at high P und T. Geochimica et Cosmochimica Acta, 101, 285-301.

Kutzschbach, M., Wunder, B., Rhede, D., Koch-Müller, M., Ertl, A., Giester, G., Heinrich, W., and Franz, G. (2016) Tetrahedral boron in natural and synthetic HP/UHP tourmaline: Evidence from Raman spectroscopy, EMPA, and single-crystal XRD. American Mineralogist, 101, 93-104.

Kutzschbach, M., Wunder, B., Trumbull, R.B., Rocholl, A., Meixner, A., and Heinrich W. (2017a) An experimental approach to quantify the effect of tetrahedral boron in tourmaline on the boron isotope fractionation between tourmaline and fluid. American Mineralogist, 102, 2505-2511.

Kutzschbach, M., Wunder, B., Krstulovic, M., Ertl, A., Trumbull, R.B., Rocholl, A., and Giester, G. (2017b) First high-pressure synthesis of rossmanitic tourmaline and evidence for the incorporation of Li at the X site. Physics and Chemistry of Minerals, 44, 353-363.

Larson, A.C., and Von Dreele, R.B. (1987) Generalized structure analysis system. Los Alamos National Laboratory Report LAUR, 86-748.

Lussier, A.J., Abdu, Y. Hawthorne, F.C., Michaelis, V.K., Aguiar, P.M., and Kroeker, C. (2011) Oscillatory zoned liddicoatite from Anjanabonoina, Central Madagascar. I. Crystal chemistry and structure by SREF and 11B and 27Al MAS NMR spectroscopy. Canadian Mineralogist, 49, 43-88.

Marler, B., Borowski, M., Wodara, U., and Schreyer, W. (2002) Synthetic tourmaline (olenite) with excess boron replacing silicon in the tetrahedral site: II. Structure analysis. European Journal of Mineralogy, 14, 763-771.

Marschall, H.R., Ertl, A., Hughes, J.M., and McCammon, C. (2004) Metamorphic Na- and OH-rich disordered dravite with tetrahedral boron, associated with omphacite, from Syros, Greece: chemistry and structure. Mineralogy and Petrology, 16(5), 817-823.

Meyer, C., Wunder, B., Meixner, A., Romer, R.L., and Heinrich, W. (2008) Boron-isotopic fractionation between tourmaline and fluid: an experimental re-investigation. Contributions to Mineralogy and Petrology, 156, 259-267.

Mirwald P.W., and Massonne H.-J. (1980) Quartz-coesite transition and the comparative friction measurements in piston-cylinder apparatus using talc-alsimag-glass (TAG) and NaCl high pressure cells: a discussion. Neues Jahrbuch Mineralogischer Monatshefte, 1980, 469-477.

Nakano, T., and Nakamura, E. (2001) Boron isotope geochemistry of metasedimentary rocks and tourmaline in a subduction zone metamorphic suite. Physics of the Earth and Planetary Interiors, 127(1), 233-252.

Schreyer, W., Wodara, U., Marler, B., Seifert, F., and Robert, J.L. (2000) Synthetic tourmaline (olenite) with excess boron replacing silicon in the tetrahedral site: I. Synthesis conditions, chemical and spectroscopic evidence. European Journal of Mineralogy, 12(3), 529-541.

Shannon, R.D. (1976) Revised effective ionic radii and systematic studies of interatomic distances in halides and chalcogenides. Acta Crystallographica, Section A, 32(5), 751-767.

Skogby, H., Bosi, F., and Lazor, P. (2012): Short-range order in tourmaline: a vibrational spectroscopic approach to elbaite. Physics and Chemistry of Minerals, 39, 811-816.

Tippe, A., and Hamilton, W.C. (1971) A neutron-diffraction study of the ferric tourmaline, buergerite. American Mineralogist, 56, 101-113.

Trumbull, R.B., Krienitz, M.-S., Grundmann, G., and Wiedenbeck, M. (2009) Tourmaline geochemsitry and $\delta^{11}B$ variations as a guide to fluid-rock interaction in the Habachtal emerald deposit, Tauern Window, Austria. Contributions to Mineralogy and Petrology, 157, 411-427.

Van Hinsberg, V. (2011) Preliminary experimental data on trace element partitioning between tourmaline an silicate melt. Canadian Mineralogist, 49(1), 153-163.

Veličkov, B. (2002) Kristallchemie von Fe, Mg-Turmalinen: Synthese und spektroskopische Untersuchungen, 175 p. Ph.D. thesis, Technische Universität Berlin, Berlin, Germany.

Vegas, A., Cano, F.H., and Garcia-Blanco, S. (1977) Refinement of aluminium orthoborate. Acta Crystallographica Section B, 33, 3607-3609.

Watenphul, A., Burgdorf, M., Schlüter, J., Horn, I., Malcharek, T., and Mihailova, B. (2016) Exploring the potential of Raman spectroscopy for crystallochemical analyses of complex hydrous silicates: II. Tourmalines. American Mineralogist, 101(4), 970-985.

Wodara, U., and Schreyer, W. (2001) X-site vacant Al-tourmaline: a new synthetic end-member. European Journal of Mineralogy, 13, 521-532.

Wunder, B., Berryman, E., Plessen, B., Rhede, D., Koch-Müller, M., and Heinrich, W. (2015) Synthetic and ammonium-bearing tourmaline. American Mineralogist, 100, 250-256.

Table captions

Table 1. Results from Rietveld refinement of powder XRD data of elbaitic, liddicoatitic and Ca-olenitic tourmaline.

Table 2. Compositions of synthetic elbaitic, liddicoatitic and Ca-olenitic tourmaline from EMP and SIMS-analyses.

Table 3. Fitting parameters and band assignment of powder Raman spectra of elbaitic and liddicoatitic tourmaline and oriented single crystal spectra of Ca-olenitic tourmaline in *-y(zz)y* scattering geometry using the approach of Gonzalez-Carreño et al. (1988)

Table 4. Comparison of site occupancies derived from EMP/SIMS, Raman and powder XRD.

Table 5. Raman intensities, Raman shifts and *-y(zz)y* / *-y(xx)y* intensity ratios of O-H bands occurring in parallel polarized single crystal spectra of Ca-olenitic tourmaline.

Table 6. Fitting parameters and band assignment of powder Raman spectra of elbaitic and liddicoatitic tourmaline and oriented single crystal spectra of Ca-olenitic, olenite and rossmanitic tourmaline in *-y(zz)y* scattering geometry using the approach of Watenphul et al. (2016)

Figure captions

Figure 1. Scanning electron microscope image of (a) elbaitic (b) liddicoatitic and (c) Ca-olenitic tourmaline.

Figure 2. Raman spectra of synthetic elbaitic, liddicoatitic and Ca-olenitic tourmaline. For elbaitic and liddicoatitic tourmaline, Raman spectra have been obtained from unoriented crystal aggregates, whereas for Ca-olenitic tourmaline a single crystal is probed in *-y(zz)y* scattering geometry. Wave numbers and assignments of bands related to O1-H vibrations are in blue font and those related to O3-H vibrations are in black font.

Figure 3. Topology of the tourmaline structure with focus on the cation configuration around O3 and O1 sites (V and W sites, respectively). For the cation occupancy indicated with an arrow typical bond distances are given. These are from a single crystal structure refinement of synthetic olenite presented in Kutzschbach et al. (2016).

Figure 4. Cation occupancies at X, Y and T sites in tourmaline as derived by Raman spectroscopy vs. results from EMP data. For all crystallographic sites, elements and tourmaline species under investigation, the data plot close to the 1:1 line, confirming the the Raman band assignment and the calculation procedure described in Kutzschbach et al. (2017b) and in the text.

Figure 5. Raman spectra of synthetic Ca-olenitic tourmaline obtained from an oriented single crystal in *-y(xx)y* scattering geometry probing the same spot as for the *-y(zz)y* spectrum presented in Fig. 2c under the same analytical conditions. For band assignment see Tables 3 and 6. For fitting parameters and *-y(zz)y* / *-y(xx)y* intensity ratios see Table 5. Wave numbers of bands related to O1-H vibrations are in blue font and those related to O3-H vibrations are in black font. The r^2 value (goodness of the fit) is 0.95.

Figure 6. Correlation of the tetrahedral B content in synthetic tourmaline determined by EMP analyses vs. the sum of the relative integrated intensities of Raman bands related to the occurrence of B at the T site. By applying the formula indicated in the top part of the graph the tetrahedral B content of any tourmaline can be calculated from the Raman spectra.

Tables

Table 1. Results from Rietveld refinement of powder XRD data of elbaitic, liddicoatitic and Ca-olenitic tourmaline.

	Refinement statistics		Cell-dimensions			Products
Sample	Durbin Watson	χ^2	$a = b$ (Å)	c (Å)	V (Å^3)	wt%
elbaitic	1.460	1.019	15.681(1)	7.054(1)	1502.2(3)	Elb (90), Coe (10)
liddicoatitic	1.497	1.009	15.604(2)	7.016(1)	1479.4(4)	Liddi (77), Coe (23)
Ca-olenitic	1.418	1.109	15.635(5)	7.027(3)	1488(1)	Ca-Ol(60), Coe(24), $AlBO_3$(16)

Uncertainties of the lattice parameters are Rietveld-determined uncertainties multiplied by six.

Table 2. Mean compositions of synthetic elbaitic, liddicoatitic and Ca-olenitic tourmaline from EMP and SIMS-analyses.

	elbaitic	liddicoatitic	Ca-olenitic
No. of analysis (n)	30 EMP/13 SIMS	20 EMP/9 SIMS	14 EMP
Na_2O (EMP)	2.39(0.18)	n.d.	n.d.
CaO (EMP)	n.d.	4.70(0.16)	2.29(0.47)
SiO_2 (EMP)	29.69(1.40)	24.97(0.70)	28.88(1.21)
Al_2O_3 (EMP)	45.24(0.79)	44.99(0.29)	47.53(0.26)
B_2O_3 (EMP)	15.71(1.08)	18.85(0.82)	16.72(1.00)
Li_2O (SIMS)	0.70(0.08)	0.58(0.11)	n.d.
H_2O	n.d.	n.d.	n.d.
Total	93.76(0.82)	94.10(0.52)	95.42(0.71)
Normalization	18 YZTB	18 YZTB	18 YZTB
T site			
Si	4.67(0.25)	3.80(0.18)	4.43(0.25)
Al	0.01(0.03)	0.01(0.03)	0.00(0.01)
B	1.31(0.25)	2.20(0.19)	1.57(0.25)
X site			
Na	0.74(0.05)	n.d.	n.d.
Ca	n.d.	0.80(0.03)	0.39(0.08)
□	0.26(0.05)	0.20(0.03)	0.61(0.08)
B site			
$^{[3]}B$	3	3	3
Y site			
Al	2.55(0.01)	2.63(0.00)	3.00(0.00)
Li	0.45(0.01)	0.37(0.00)	n.d.
Z site			
Al	5.94(0.07)	5.83(0.09)	5.86(0.08)
Si	0.06(0.07)	0.17(0.09)	0.14(0.08)
V + W site			
OH	3.41(0.24)	3.17(0.12)	2.65(0.10)
O	0.59(0.24)	0.83(0.12)	1.35(0.10)

Error on oxides determined by EMP is indicated in brackets and is 1SD from the mean of n measurements. Stoichiometric tourmaline formulae were calculated for each individual analysis by normalizing the Y+Z+T+B cations to a total of 18 and using a fixed Li_2O content as determined by SIMS. All Li is assigned to the Y site. The error for the cation proportion is indicated in brackets and is 1 SD from the mean of n formula derived from the EMP+SIMS data.

Table 3. Fitting parameters and band assignment of powder Raman spectra of elbaitic and liddicoatitic tourmaline and oriented single crystal spectra of Ca-olenitic tourmaline in *-y(zz)y* scattering geometry using the approach of Gonzalez-Carreño et al. (1988)

Band	Raman shift (cm^{-1})	FWHM (cm^{-1})	I_{rel} (%)	Assignment	O3/O1
elbaitic					
ν_1	3294(2)	53(6)	2.3(1.0)	$^{Z}(AlAl)^{Y}(Al)^{T}(Si,B)^{X}\square$	O3
ν_2	3369(1)	94(2)	46.2(2.6)	$^{Z}(AlAl)^{Y}(Al)^{T}(Si,B)\,^{X}Na$	O3
ν_3	3454(1)	51(2)	12.2(1.5)	$^{Z}(AlAl)^{Y}(Al)^{T}(Si)^{X}\square$	O3
ν_4	3496(1)	57(1)	32.2(2.2)	$^{Z}(AlAl)^{Y}(Al)^{T}(Si)\,^{X}Na$	O3
ν_5	3564(2)	35(4)	1.5(0.5)	$^{X}\square\,^{Y}(AlAlAl)$	O1
ν_6	3601(1)	35(2)	4.4(0.8)	$^{Z}(AlAl)^{Y}(Li)^{T}(Si)\,^{X}Na$	O3
ν_7	3630(1)	17(2)	0.4(0.3)[a]	$^{X}\square\,^{Y}(LiAlAl)$	O1
ν_8	3657(1)	21(1)	0.8(0.2)	$^{X}Na^{Y}(LiAlAl)$	O1
liddicoatitic					
ν_1	3316(1)	125(1)	18.9(2.0)	$^{Z}(AlAl)^{Y}(Al)^{T}(Si,B)^{X}\square$	O3
ν_2	3430(2)	82(2)	52.0(4.5)	$^{Z}(AlAl)^{Y}(Al)^{T}(Si,B)\,^{X}Ca$	O3
ν_3	3469(1)	49(5)	6.5(2.9)	$^{Z}(AlAl)^{Y}(Al)^{T}(Si)^{X}\square$	O3
ν_4	3533(1)	57(3)	15.1(2.2)	$^{Z}(AlAl)^{Y}(Al)^{T}(Si)\,^{X}Ca$	O3
ν_5	3584(3)	50(10)	3.0(1.4)	$^{X}\square\,^{Y}(AlAlAl)$	O1
ν_6	3623(1)	33(3)	3.8(1.3)	$^{Z}(AlAl)^{Y}(Li)^{T}(Si)\,^{X}Ca$	O3
ν_7	3648(1)	20(2)	0.8(0.1)	$^{X}\square\,^{Y}(LiAlAl)$	O1
Ca-olenitic					
ν_1	3288(1)	108(2)	24.5(2.9)	$^{Z}(AlAl)^{Y}(Al)^{T}(Si,B)^{X}\square$	O3
ν_2	3423(6)	75(5)	23.5(4.4)	$^{Z}(AlAl)^{Y}(Al)^{T}(Si,B)\,^{X}Ca$	O3
ν_3	3451(2)	60(1)	43.2(5.2)	$^{Z}(AlAl)^{Y}(Al)^{T}(Si)^{X}\square$	O3
ν_4	3528(1)	30(2)	2.8(0.8)	$^{Z}(AlAl)^{Y}(Al)^{T}(Si)\,^{X}Ca$	O3
ν_5	3573(1)	48(3)	4.3(1.3)	$^{X}\square\,^{Y}(AlAlAl)$	O1
ν_6	3630(1)	35(2)	1.7(0.6)	$^{X}Ca^{Y}(AlAlAl)$	O1

Error on Raman shift and FWHM (in brackets) is 1 SD as derived from the fit. Error on relative integrated intensities (in brackets) have been calculated by propagating the 1 SD errors on integrated intensities as derived from the fit.

[a] included due to shoulder at higher wavenumber side of band ν_6 although relative intensity threshold is violated.

Table 4. Comparison of site occupancies derived from EMP/SIMS, Raman and powder XRD

	Site	EMP/SIMS	Raman	XRD (from V[f])
elbaitic	X	$Na_{0.74(5)}$	$Na_{0.85(3)}$[a]	
			$Na_{0.67(23)}$[b,c]	
	Y	$Li_{0.45(1)}$	$Li_{0.21(20)}$[b,d]	
	T	$B_{1.31(25)}$	$B_{1.50(12)}$[a]	$B_{1.36(1)}$
liddicoatitic	X	$Ca_{0.80(3)}$	$Ca_{0.74(5)}$[a]	
			--- [b,e]	
	Y	$Li_{0.37(1)}$	$Li_{0.21(15)}$[b,d]	
	T	$B_{2.20(19)}$	$B_{2.21(20)}$[a]	$B_{2.14(1)}$
Ca-olenitic	X	$Ca_{0.39(8)}$	$Ca_{0.28(7)}$[a]	
			$Ca_{0.28(15)}$[b]	
	T	$B_{1.57(25)}$	$B_{1.53(21)}$[a]	$B_{1.85(4)}$

Cation occupancies have been calculated using the procedure described in Kutzschbach et al. (2017). A short explanation is also given in the text. The errors of site occupancies have been calculated by propagating the 1SD errors of the relative integrated intensities presented in Table 3. Please note that errors are slightly overestimated by that procedure.

[a] calculation based on assignment of the O3-H vibrations

[b] calculation based on assignment of the O1-H vibrations

[c] simplified calculation using the ratio $I_{rel}(\nu_8)/[(I_{rel}(\nu_8)+ I_{rel}(\nu_7)]$. For a more accurate calculation the relative integrated intensity of the band related to the configuration $^{X}Na^{Y}$(AlAlAl) is needed, which is probably superimposed by band ν_6

[d] simplified calculation based on relative integrated intensities ratio $I_{rel}(\nu_7)/[(I_{rel}(\nu_5)+ I_{rel}(\nu_7)]$. The Li content is likely underestimated because some intensity of ν_5 is due to the O3-H band related to the configuration $^{Z}(AlAl)^{Y}(Li)^{T}(Si)^{X}\square$

[e] not detected probably due to deprotonation (for further information see text)

[f] after Ertl et al. (2018) $^{[4]}B = (V\text{-}1542)/(-29.242)$

Table 5. Raman intensities, Raman shifts and *-y(zz)y* / *-y(xx)y* intensity ratios of O-H bands occurring in parallel polarized single crystal spectra of Ca-olenitic tourmaline.

Band	O3/O1	*-y(zz)y*		*-y(xx)y*		Intensity ratio
		Intensity	Shift	Intensity	Shift	*-y(zz)y* / *-y(xx)y*
ν_1	O3	37182 (944)	3288 (1)	2404 (350)	3292 (6)	15 (3)
ν_2	O3	35691 (5476)	3423 (6)	2416 (494)	3402 (1)	15 (6)
ν_3	O3	65586 (6907)	3451 (2)	4853 (1417)	3451 (1)	14 (6)
ν_4	O3	4227 (832)	3528 (1)	487 (755)	3519 (2)	--[a]
ν_5	O1	6557 (1357)	3573 (1)	2593 (1865)	3568 (3)	--[a]
ν_6	O1	2637 (601)	3630 (1)	4393 (1033)	3624 (2)	0.6 (3)

Intensities are indicated as integrated counts. Raman spectra have been acquired at the same spot of the same single crystal under the same analytical conditions but with different scattering geometries obtained by 90° rotation the crystal about the *y* axis. For raw intensities, numbers in brackets denote the error (1 SD) as derived from the fit. For the intensity ratios errors (1 SD) and have been derived from error propagation

[a]no indication of intensity ratio due to the large error on intensities for the *-y(xx)y* scattering geometry, which are far off the band criterion, i.e. $\Delta I/I >> 0.5$

Table 6. Fitting parameters and band assignment of powder Raman spectra of elbaitic and liddicoatitic tourmaline and oriented single crystal spectra of Ca-olenitic, olenite and rossmanitic tourmaline in *-y(zz)y* scattering geometry using the approach of Watenphul et al. (2016)

Band	Raman shift (cm^{-1})	FWHM (cm^{-1})	I_{rel} (%)	Assignment	O3/O1
Elbaitic					
ν_1	3294(2)	53(6)	2.3(1.0)	(□-AlAlAl-AlAlAl-AlAlAl)$^{(Si,B)}$	O3
ν_2	3369(1)[a]	94(2)	46.2(2.6)	(Na-AlAlAl-AlAlAl-AlAlAl)$^{(Si,B)}$	O3
				((□,Na)-LiAlAl-AlAlAl-AlAlAl)$^{(Si,B)}$	
ν_3	3454(1)	51(2)	12.2(1.5)	(□-AlAlAl-AlAlAl-AlAlAl)$^{(Si)}$	O3
ν_4	3496(1)	57(1)	32.2(2.2)	((□,Na)-LiAlAl-AlAlAl-AlAlAl)$^{(Si)}$	O3
				(Na)-AlAlAl-AlAlAl-AlAlAl)$^{(Si)}$	
ν_5	3564(2)	35(4)	1.5(0.5)	□-AlAlAl	O1
ν_6	3601(1)	35(2)	4.4(0.8)	Na-AlAlAl	O1
ν_7	3630(1)	17(2)	0.4(0.3)[a]	□-LiAlAl	O1
ν_8	3657(1)	21(1)	0.8(0.2)	Na-LiAlAl	O1
liddicoatitic					
ν_1	3316(1)	125(1)	18.9(2.0)	(□-AlAlAl-AlAlAl-AlAlAl)$^{(Si,B)}$	O3
ν_2	3430(2)	82(2)	52.0(4.5)	(Ca-AlAlAl-AlAlAl-AlAlAl)$^{(Si,B)}$	O3
				((□,Ca)-LiAlAl-AlAlAl-AlAlAl)$^{(Si,B)}$	O3
ν_3	3469(1)	49(5)	6.5(2.9)	(□-AlAlAl-AlAlAl-AlAlAl)$^{(Si)}$	
ν_4	3533(1)	57(3)	15.1(2.2)	((□,Ca)-LiAlAl-AlAlAl-AlAlAl)$^{(Si)}$	O3
				(Ca-AlAlAl-AlAlAl-AlAlAl)$^{(Si)}$	
ν_5	3584(3)	50(10)	3.0(1.4)	□-AlAlAl	O1
ν_6	3623(1)	33(3)	3.8(1.3)	Ca-AlAlAl	O1
ν_7	3648(1)	20(2)	0.8(0.1)	□-LiAlAl	O1
Ca-olenitic					
ν_1	3288(1)	108(2)	24.5(2.9)	(□-AlAlAl-AlAlAl-AlAlAl)$^{(Si,B)}$	O3
ν_2	3423(6)	75(5)	23.5(4.4)	(Ca-AlAlAl-AlAlAl-AlAlAl)$^{(Si,B)}$	O3
ν_3	3451(2)	60(1)	43.2(5.2)	(□-AlAlAl-AlAlAl-AlAlAl)$^{(Si)}$	O3
ν_4	3528(1)	30(2)	2.8(0.8)	(Ca-AlAlAl-AlAlAl-AlAlAl)$^{(Si)}$	O3
ν_5	3573(1)	48(3)	4.3(1.3)	□-AlAlAl	O1
ν_6	3630(1)	35(2)	1.7(0.6)	Ca-AlAlAl	O1

Table 6. continued

Olenite[b]					
ν_1	3284(6)	103(20)	16(3)	(□-AlAlAl-AlAlAl-AlAlAl)$^{(Si,B)}$	O3
ν_2	3370(4)	89(4)	27(4)	(Na-AlAlAl-AlAlAl-AlAlAl)$^{(Si,B)}$	O3
ν_3	3451(3)	56(4)	42(4)	(□-AlAlAl-AlAlAl-AlAlAl)$^{(Si)}$	O3
ν_4	3498(5)	49(5)	12(3)	(Na-AlAlAl-AlAlAl-AlAlAl)$^{(Si)}$	O3
ν_5	3554(2)	27(2)	0.8(0.1)	□-AlAlAl	O1
ν_6	3602(1)	43(14)	2.1(0.8)	Na-AlAlAl	O1
Rossmanitic[c]					
ν_1	3311(1)	97(1)	13.4(0.4)	(□-AlAlAl-AlAlAl-AlAlAl)$^{(Si,B)}$	O3
ν_2	3394(1)	45(5)	1.4(0.3)	((□,Li)-LiAlAl-AlAlAl-AlAlAl)$^{(Si,B)}$	O3
				(Li-AlAlAl-AlAlAl-AlAlAl)$^{(Si,B)}$	
ν_3	3452(1)	59(1)	65.3(1.3)	(□-AlAlAl-AlAlAl-AlAlAl)$^{(Si)}$	O3
ν_4	3574(1)	51(1)	14.5(0.6)	((□,Li)-LiAlAl-AlAlAl-AlAlAl)$^{(Si)}$	O3
				(Li-AlAlAl-AlAlAl-AlAlAl)$^{(Si)}$	
ν_5	3620(2)	34(5)	1.5(0.5)	□-AlAlAl	O1
ν_6	3648(1)	17(3)	0.8(0.3)	Li-AlAlAl	O1
ν_7	3668(1)	16(1)	2.7(0.2)	□-LiAlAl	O1
ν_8	3706(1)	11(1)	0.5(0.1)	Li-LiAlAl)	O1

Error on Raman shift and FWHM (in brackets) is 1 SD as derived from the fit. Error on relative integrated intensities (in brackets) have been calculated by propagating the 1 SD errors on integrated intensities as derived from the fit. Assigment for ^{V}OH modes refers to (X-YZZ-YZZ-YZZ)^{T} configurations with X= vacancy (□), Na, Li, Ca; T = Si or (Si,B) meaning either Si_6O_{18} or $Si_3B_3O_{18}$ rings. Assignments for ^{W}OH modes refers to X-YYY configurations

[a] included due to shoulder at higher wavenumber side of band ν_6 although relative intensity threshold is violated.

[b] re-assignment of Raman spectrum of olenite (columnar variety) presented in Kutzschbach et al. 2016

[c] re-assignment of Raman spectrum of rossmanitic tourmaline presented in Kutzschbach et al. 2017

Figure 1

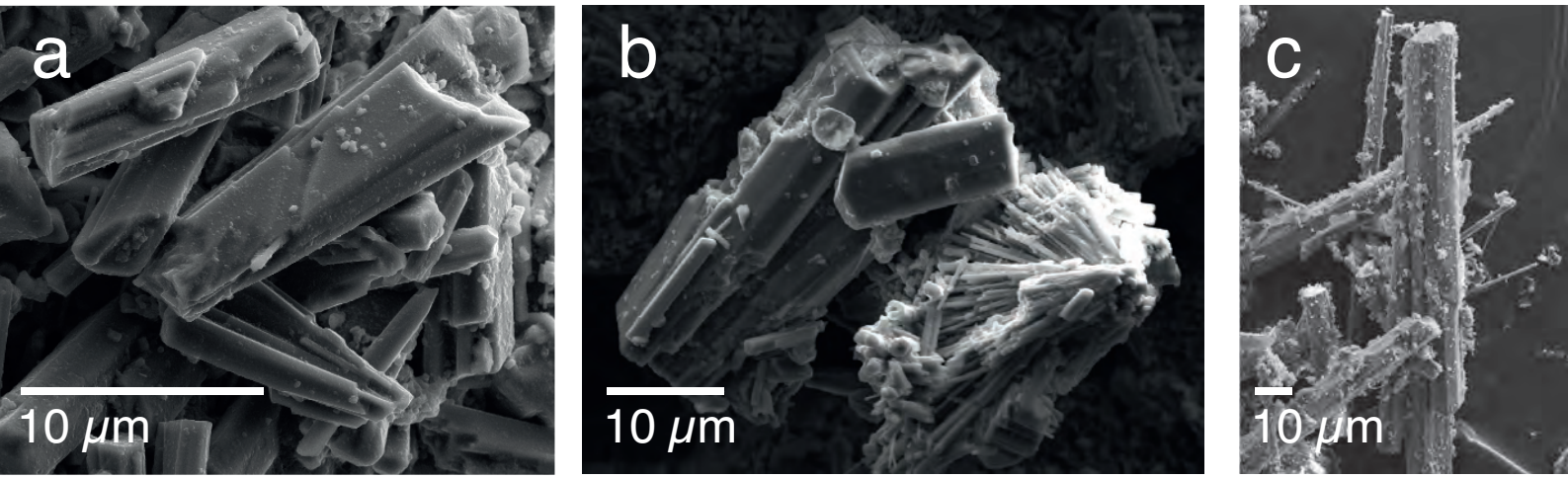

Figure 2

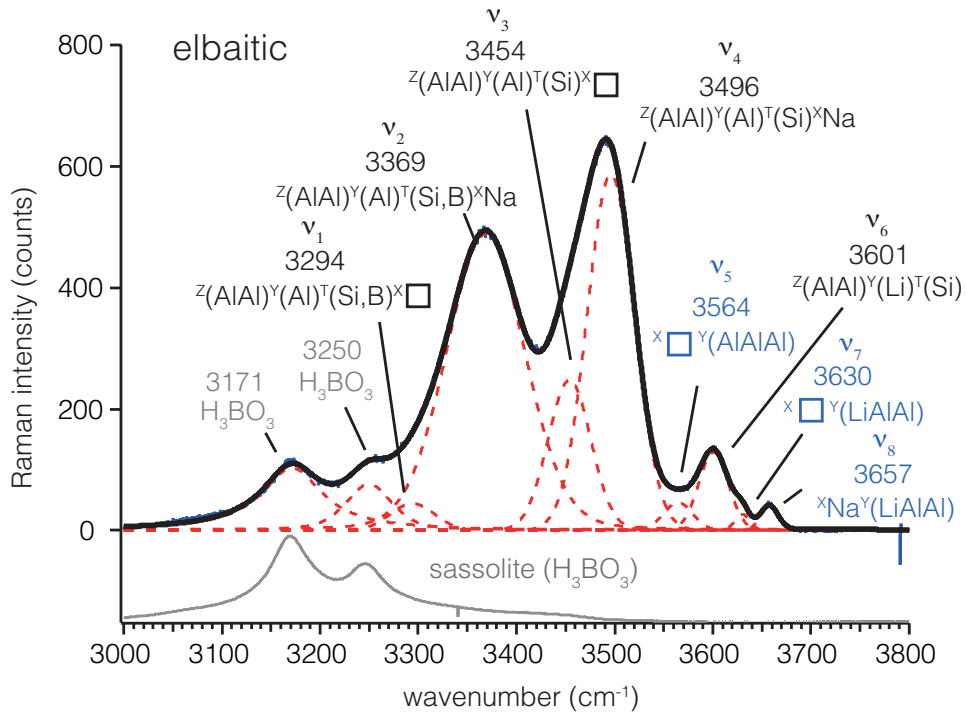
elbaitic
ν3
3454
Z(AlAl)Y(Al)T(Si)X□
ν4
3496
Z(AlAl)Y(Al)T(Si)XNa
ν2
3369
Z(AlAl)Y(Al)T(Si,B)XNa
ν1
3294
Z(AlAl)Y(Al)T(Si,B)X□
ν5
3564
X□Y(AlAlAl)
ν6
3601
Z(AlAl)Y(Li)T(Si)
ν7
3630
X□Y(LiAlAl)
ν8
3657
XNaY(LiAlAl)
3250
H3BO3
3171
H3BO3
sassolite (H3BO3)
Raman intensity (counts)
wavenumber (cm-1)

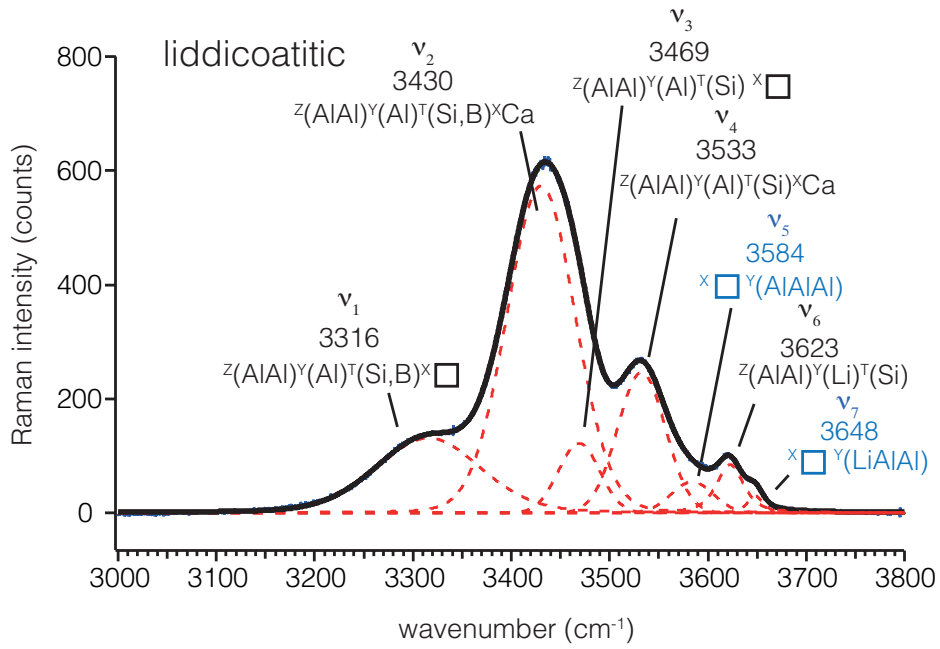
liddicoatitic
ν3
3469
Z(AlAl)Y(Al)T(Si) X□
ν2
3430
Z(AlAl)Y(Al)T(Si,B)XCa
ν4
3533
Z(AlAl)Y(Al)T(Si)XCa
ν5
3584
X□Y(AlAlAl)
ν1
3316
Z(AlAl)Y(Al)T(Si,B)X□
ν6
3623
Z(AlAl)Y(Li)T(Si)
ν7
3648
X□Y(LiAlAl)
Raman intensity (counts)
wavenumber (cm-1)

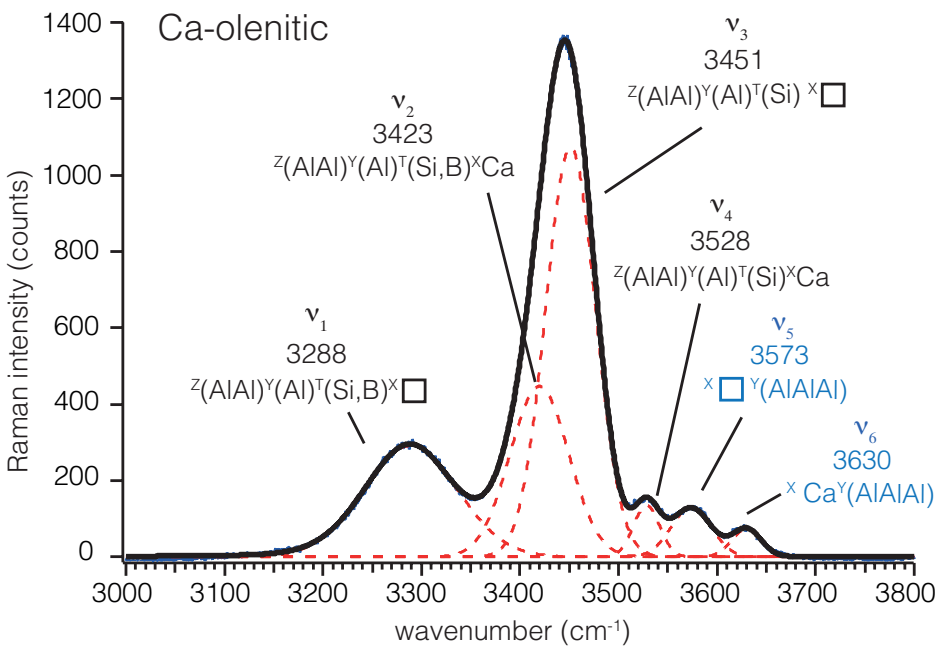
Ca-olenitic
ν3
3451
Z(AlAl)Y(Al)T(Si) X□
ν2
3423
Z(AlAl)Y(Al)T(Si,B)XCa
ν4
3528
Z(AlAl)Y(Al)T(Si)XCa
ν1
3288
Z(AlAl)Y(Al)T(Si,B)X□
ν5
3573
X□Y(AlAlAl)
ν6
3630
X CaY(AlAlAl)
Raman intensity (counts)
wavenumber (cm-1)

Figure 3

Configuration around O3 site

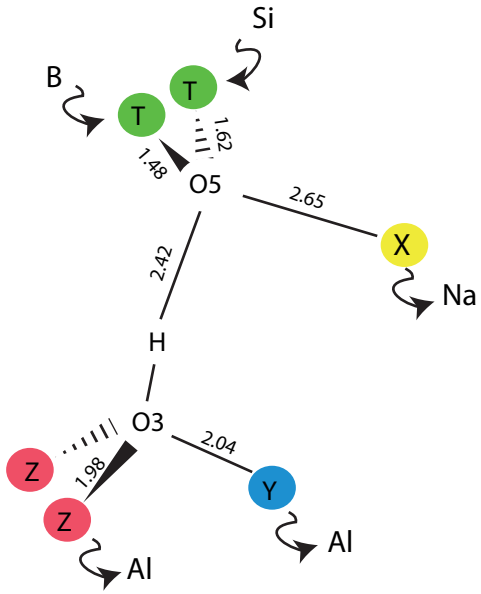

Configuration around O1 site

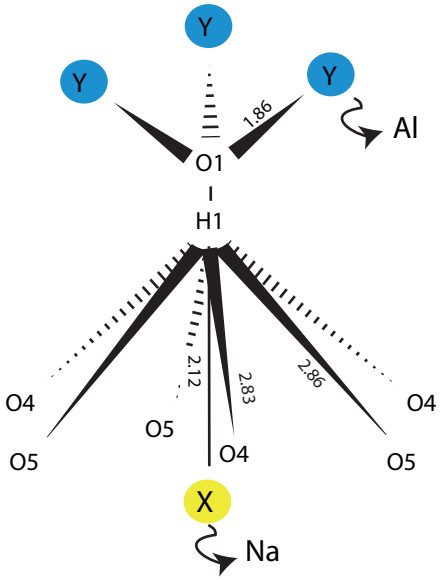

Figure 4

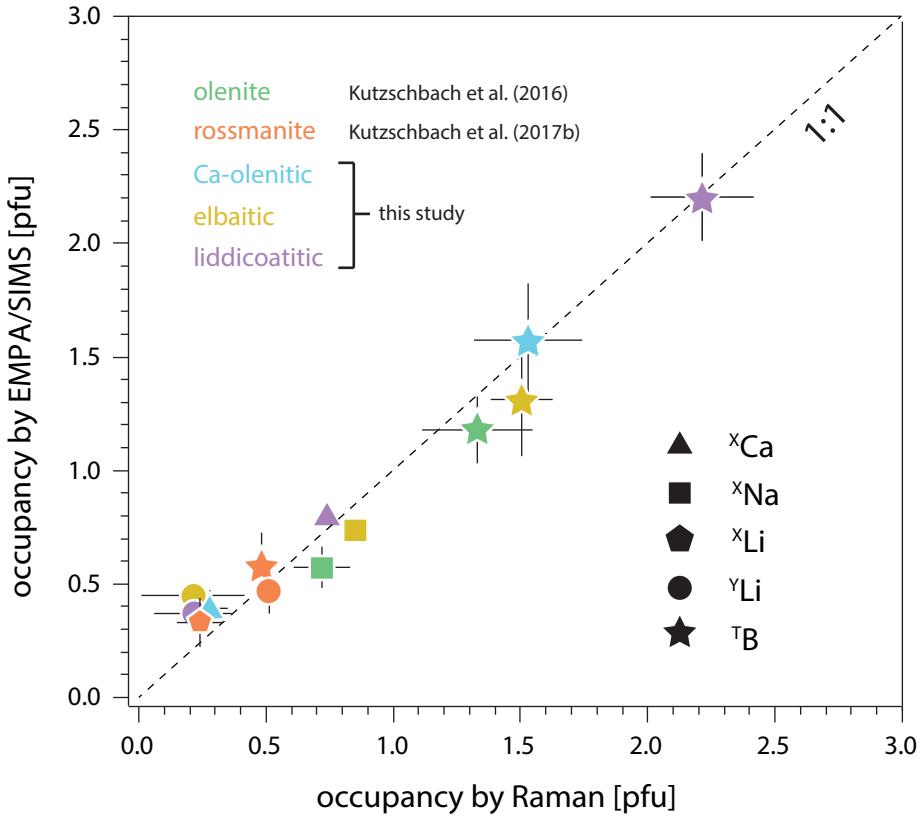
3.0
2.5
2.0
1.5
1.0
0.5
0.0
0.0
0.5
1.0
1.5
2.0
2.5
3.0
occupancy by EMPA/SIMS [pfu]
occupancy by Raman [pfu]
olenite
Kutzschbach et al. (2016)
rossmanite
Kutzschbach et al. (2017b)
Ca-olenitic
elbaitic
liddicoatitic
this study
1:1
XCa
XNa
XLi
YLi
TB

Figure 5

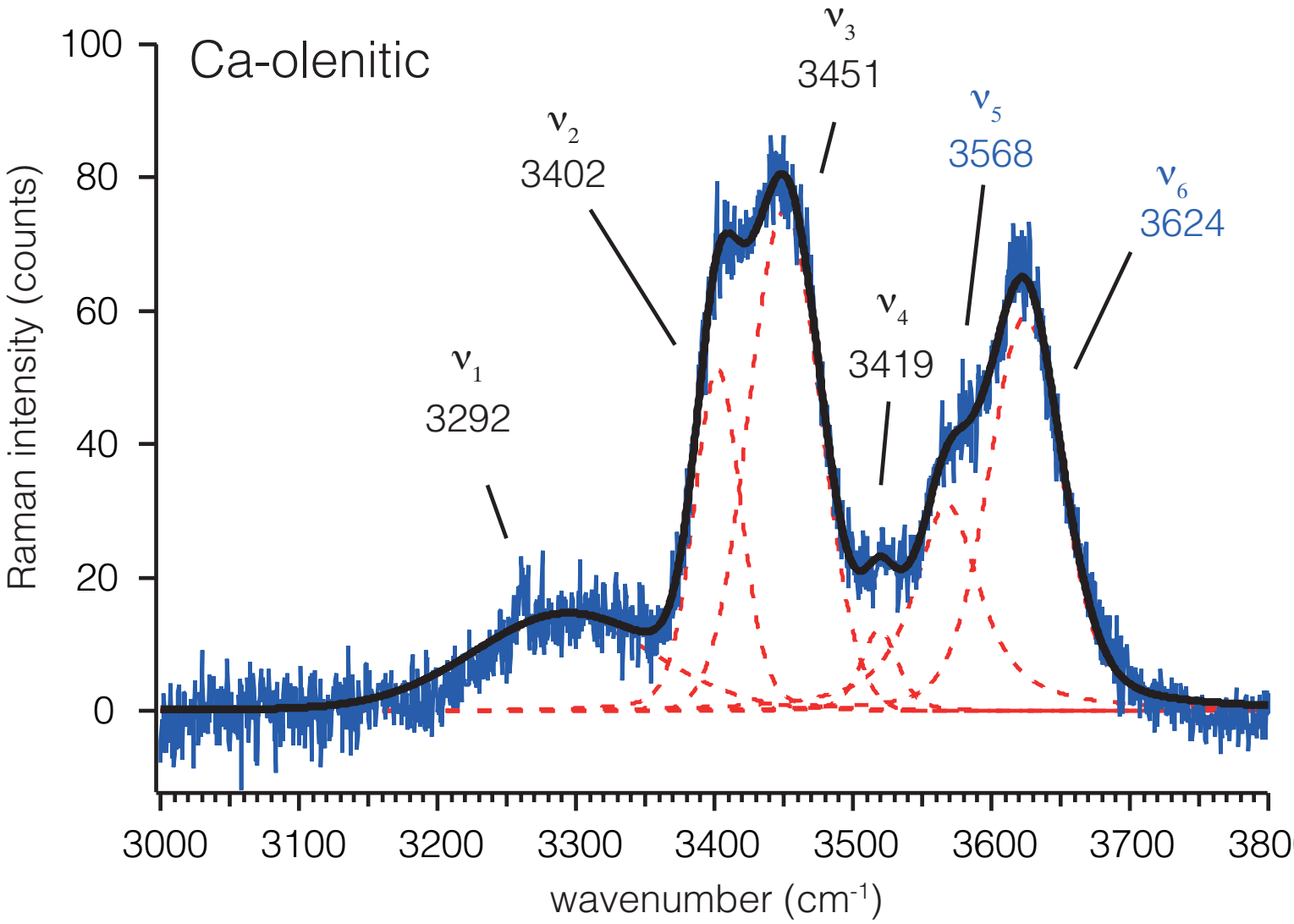
Ca-olenitic
ν1
3292
ν2
3402
ν3
3451
ν4
3419
ν5
3568
ν6
3624
Raman intensity (counts)
100
80
60
40
20
0
3000
3100
3200
3300
3400
3500
3600
3700
3800
wavenumber (cm-1)

Figure 6

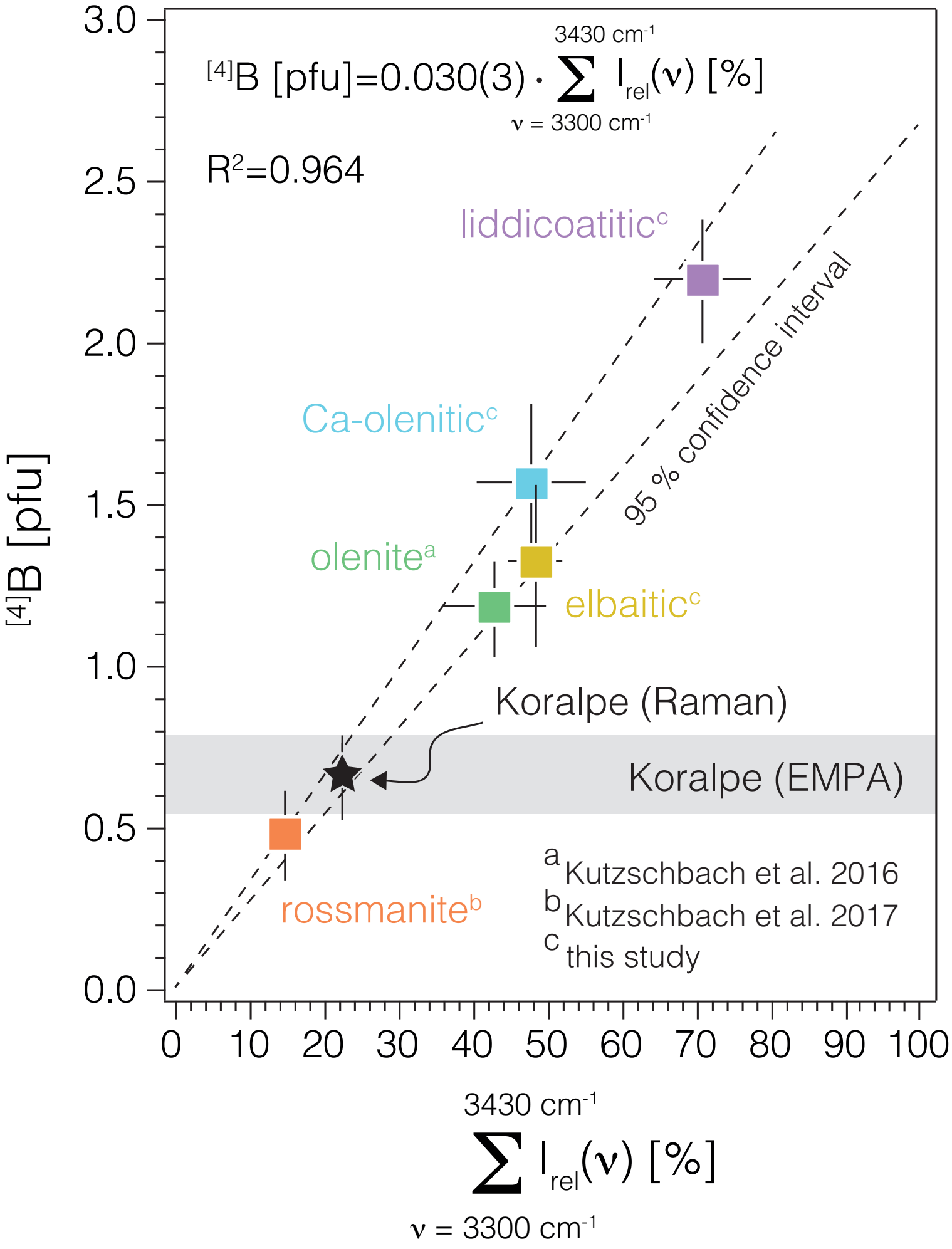
[4]B [pfu]=0.030(3) · Σ 3430 cm-1 ν = 3300 cm-1 Irel(ν) [%]
R2=0.964
liddicoatitic c
Ca-olenitic c
olenite a
elbaitic c
95 % confidence interval
Koralpe (Raman)
Koralpe (EMPA)
rossmanite b
a Kutzschbach et al. 2016
b Kutzschbach et al. 2017
c this study
[4]B [pfu]
3.0
2.5
2.0
1.5
1.0
0.5
0.0
0
10
20
30
40
50
60
70
80
90
100
3430 cm-1
Σ Irel(ν) [%]
ν = 3300 cm-1